Doctor of Philosophy

Magnetic Energy Transport through Chromospheric Spicule Revealed with Lyman-Alpha Spectro-Polarimetric Observation

Masaki Yoshida

Department of Astronomical Science
School of Physical Sciences
The Graduate University for Advanced Studies, SOKENDAI

March 12, 2020

Abstract

The solar chromosphere is the middle layer between the photosphere and the corona and is an important atmospheric layer for investigating the process of energy transfer from the photosphere to the corona. As a candidate for the energy transport mechanism, a wave heating mechanism is considered in which waves generated by convective motion in the photosphere propagate upward along the magnetic field line and dissipate their energy in the corona. For the wave heating mechanism, the velocity and magnetic fields of the chromosphere are the critical physical quantities that must be observationally determined to evaluate quantitatively the energy flux transported to the corona. Spicules, which are jet-like structures found in the chromosphere, are useful for investigating the wave propagation process in detail. The spicule is supposed to have a fibril structure along the magnetic field lines, and its lateral motion represents the movement of the magnetic field lines. To study the dynamics and magnetic properties of the upper chromosphere, including the spicule, we use unprecedentedly high-quality spectro-polarimetric data of the hydrogen Lyα line (121.6 nm) at a high temporal cadence of 0.3 s. These data were obtained from the Chromospheric Lyman-Alpha Spectro-Polarimeter (CLASP) sounding rocket experiment conducted in September 2015. CLASP performed sit-and-stare observations of the quiet Sun near the limb for about 5 minutes with a slit that was positioned perpendicular to the limb and successfully captured an off-limb spicule evolving along the slit. Note that the Lyα line is well suited for investigating how spicules affect the corona because it is sensitive to higher temperatures than other chromospheric lines because of its large optical thickness. Another advantage of this spectral line is that it is sensitive to the Hanle effect, that is, the modification of a scattering polarization by the magnetic field. In this study, we report the first detection of a high-frequency wave in line-of-sight Doppler velocity and of scattering polarization that can be used to constrain the magnetic field information through the Hanle effect from the spicule in the Lyα line.

From the time sequence data of the Lyα line spectra in 0.3 s cadences, we found high-frequency oscillations of the Doppler velocity with periods of 20–50 s and low-frequency oscillations of periods of about 240 s on the spicule. From a wavelet analysis of the time sequence data of the Doppler velocity, we also found that, in the early phase of the spicule evolution, waves with a period of about 30 s and a velocity amplitude of 2–3 $\mathrm{km\ s^{-1}}$ propagated upward along the spicule with a phase velocity of approximately 470 $\mathrm{km\ s^{-1}}$. By contrast, possible downward and standing waves with lower velocity amplitudes were also observed in the later phase. Because the period of the low-frequency wave is comparable to the observation time of CLASP, we could not confirm whether the low-frequency oscillation was propagating or not. The high frequency waves observed in the early phase of spicule evolution may be related to the onset and formation of spicules. Our analysis enabled us to identify the upward, downward, and standing waves along the spicule and to obtain the velocity amplitude of each wave directly from the Doppler velocity for the first time.

From the spectro-polarimetric data, we succeeded in detecting linear polarization of the Lyα line in the off-limb spicule for the first time with an accuracy of approximately 0.1–0.3%. The polarization in the off-limb spicule is mainly generated by a radiation field, and the direction and degree of polarization are further changed by a magnetic field (i.e., the Hanle effect). To evaluate the Hanle effects, we investigated the height and temporal variations of the Stokes polarization vectors Q/I (where a positive Q/I indicates polarization parallel to the limb) and U/I (where positive is 45° counterclockwise from Stokes Q) in the spicule. We found that at a height where the spicule can be spatially resolved as a single structure (i.e. at the upper part of the spicule), the Q/I was constant with time at a level of $+0.5\%$, and U/I changed from $+0.5\%$ to -0.5% during a period of about 240 s. The positive Q/I value indicates that 90° scattering of the incident radiation from the solar disk is dominant. The temporal variation of the U/I was correlated with the swaying motion of the spicule with respect to the slit position, which was found from the Lyα filter image obtained by the CLASP slit-jaw imager. We compared the calculated

polarization signal with the observed signal, assuming an axisymmetric radiation field. We found that the calculated temporal variation of the magnetic field angle induced by the U/I signal did not meet the spicule oscillation obtained from the spectroscopic data, and the observation result could not be explained solely by the axisymmetric radiation field. Because the spicule sways with respect to the fixed slit position, the slit position moves on the spicule from the right to the left. This means that the U/I may arise from the scattering of a skewed incident radiation field to the cylindrical spicule. As a result, it is considered that U/I changed with time because of the swaying motion of the spicule with respect to the slit position. The CLASP observation suggests that, to explain the observation of the polarization signal in the Lyα line, considering the Hanle effect with a skewed incident radiation field is necessary.

The high- and low-frequency oscillations were found from the CLASP observations. Because the high-frequency oscillation propagated at approximately a typical Alfvén velocity and its magnetic field strength (approximately 13 G) calculated from the propagation velocity and the previously derived density met a typical field strength of the spicule, the high-frequency wave was estimated to be an MHD kink wave. The energy flux of high-frequency wave was estimated to be approximately 3×10^4 erg cm^{-2} s^{-1} when using the velocity amplitude, propagation velocity, and density of the spicule, where the energy flux was insufficient for heating the quiet corona. Assuming that the spicule aligns along the magnetic field line, we found that the spicule oscillated as an MHD wave of transverse kink mode from the low-frequency oscillation in the line-of-sight and plane-of-sky direction. Because the propagation velocity is determined by the density and strength of the magnetic field in the spicule and does not depend on the period, the propagation velocity of the low-frequency wave could be regarded as the same as that of the high-frequency wave. The energy flux of the low-frequency wave was estimated to be approximately 2×10^6 erg cm^{-2} s^{-1}, which was sufficient to heat the quiet corona.

In summary, we found for the first time clear evidence for a high-frequency (30 s) propagating wave and a low-frequency (240 s) oscillation of the line-of-sight Doppler ve-

locity from the Lyα line on the spicule, which are critical for quantitatively estimating the energy flux of MHD kink waves to the corona. We also found a clear linear polarization signal of the Lyα line at a level of 0.5% from the spicule and suggested that, to derive the magnetic field from the polarization, we must develop a diagnostic tool to interpret the Hanle effect in a skewed incident radiation field to the spicule.

Contents

Chapter 1

Introduction

1.1 Solar Atmosphere

As shown in Figure 1.1, the solar atmosphere consists of four regions with different physical properties. The lowest is a thin layer several hundred kilometers thick called the photosphere. Nearly all the solar radiation we receive is emitted from this region, and its spectrum corresponds to approximately $5770\ \mathrm{K}$ of the black body radiation. Above the photosphere is a layer called the chromosphere with a temperature of about $10,000\ \mathrm{K}$, which can be glimpsed for a few seconds at the second and third contacts of a total solar eclipse as a pinkish layer. The corona reaches a million degrees over short distances through a thin transition layer above the chromosphere called the transition region, forming the supersonic solar wind and filling the heliosphere. Figure 1.1 shows that the temperature of the atmosphere steadily decreases up to a height of around $6 \times 10^2\ \mathrm{km}$, but rises to about $10^4\ \mathrm{K}$ above it. The temperature increases rapidly at about $2\text{–}3 \times 10^3\ \mathrm{km}$ (transition region), and above it, the temperature rises with decreasing density (corona).

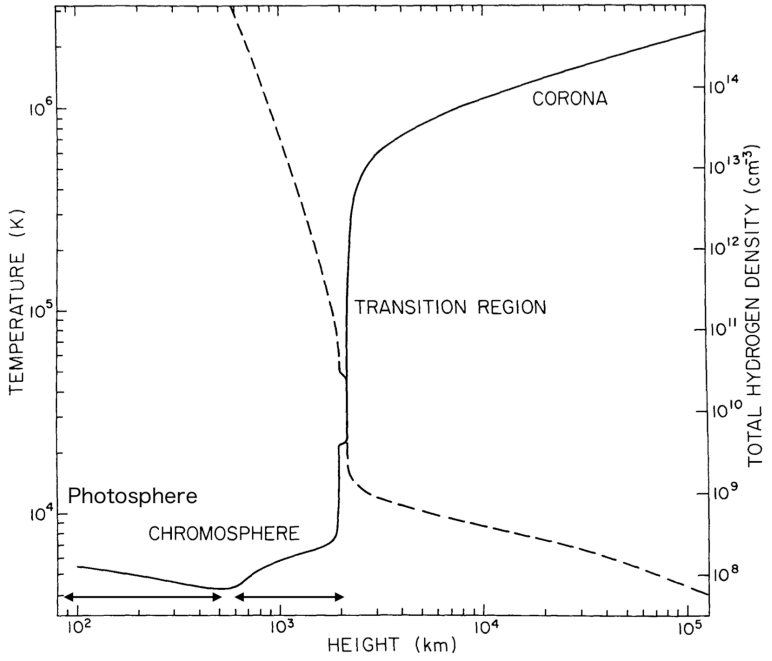

Figure 1.1: One dimensional temperature (solid line) and density (dashed line) structure above the photosphere ($\sim 10^2$ km height) in quiet region. Figure adapted from Withbroe & Noyes (1977).

1.2 Coronal Heating Problem

1.2.1 Overview

In the 1940s, the Fe X line (637.4 nm) and the Fe XIV (530.3 nm) were found by spectroscopic observations in the visible wavelength (Edlén, 1943). The observation of these high ionization lines revealed that the corona has a high temperature of about 10^6 K. Since the energy source is at the center of the Sun, heat will flow from the central region to a colder outer space; thus, the temperature should decrease as the heat moves outward in a radial direction. However, the temperature of the outer atmosphere above the photosphere increases towards the corona by two orders of magnitude. Therefore, this spectroscopic observation suggests that energy is transported from the photosphere

by certain non-thermal mechanisms and is dissipated in the upper atmosphere. These processes have been studied for many years as the "coronal heating problem," which is a big mystery in solar physics.

The energy required for heating the corona is calculated by converting the loss due to X-rays, ultraviolet radiations, heat flow into the transition region, and solar wind. Table 1.1 summarizes the energy flux required for heating in each region of the solar corona: the quiet sun corona, coronal hole, and active region corona.

Table 1.1: Total energy loss from the corona. Values adapted from Withbroe & Noyes (1977).

Total loss ($\mathrm{erg\ cm^{-2}\ s^{-1}}$)	Quiet Sun	Coronal hole	Active region
Corona	3×10^5	8×10^5	1×10^7

In the photosphere, cellar patterns called granules (500–$2000\ \mathrm{km}$) are seen. These granules are turbulent convective flows formed when energy is transported from the interior to the surface. The convective velocity is estimated using the apparent horizontal motions as 1–2 $\mathrm{km\ s^{-1}}$, and the energy flux of the convective motion is estimated as approximately $10^8\ \mathrm{erg\ cm^{-2}\ s^{-1}}$ (Alfvén, 1947), assuming photospheric density. Alfvén (1947) also assumed the propagation velocity to be the Alfvén velocity, based on the photospheric density and magnetic field strength, although it is not clear whether it propagates upward. Recent observations with high spatial resolution by the *Hinode* satellite (Kosugi et al., 2007) also suggests similar results (Matsumoto & Kitai, 2010). Therefore, only 0.1% of the energy involved in the convective flows is equivalent to the heating required for the quiet region corona.

The magnetic field plays an important role in heating the solar atmosphere since the temperature of the corona is observed to increase in the region where the strength of the photospheric magnetic field increase (Figure 1.2). Especially in the upper chromosphere to the corona, the plasma-β, which is the ratio of the gas pressure to magnetic pressure, becomes smaller than unity (Figure 1.3). In this region, the plasma motion is governed by the magnetic field. Solving the coronal heating problem requires a quantitative un-

derstanding of three processes: magnetic energy generation, transportation, and dissipation. The magnetic heating mechanisms that have been proposed so far are classified into two; the first, micro-flares, caused by small-scale magnetic reconnections, and the second caused by wave heating mechanisms. In the following subsections, we explain these two mechanisms in detail.

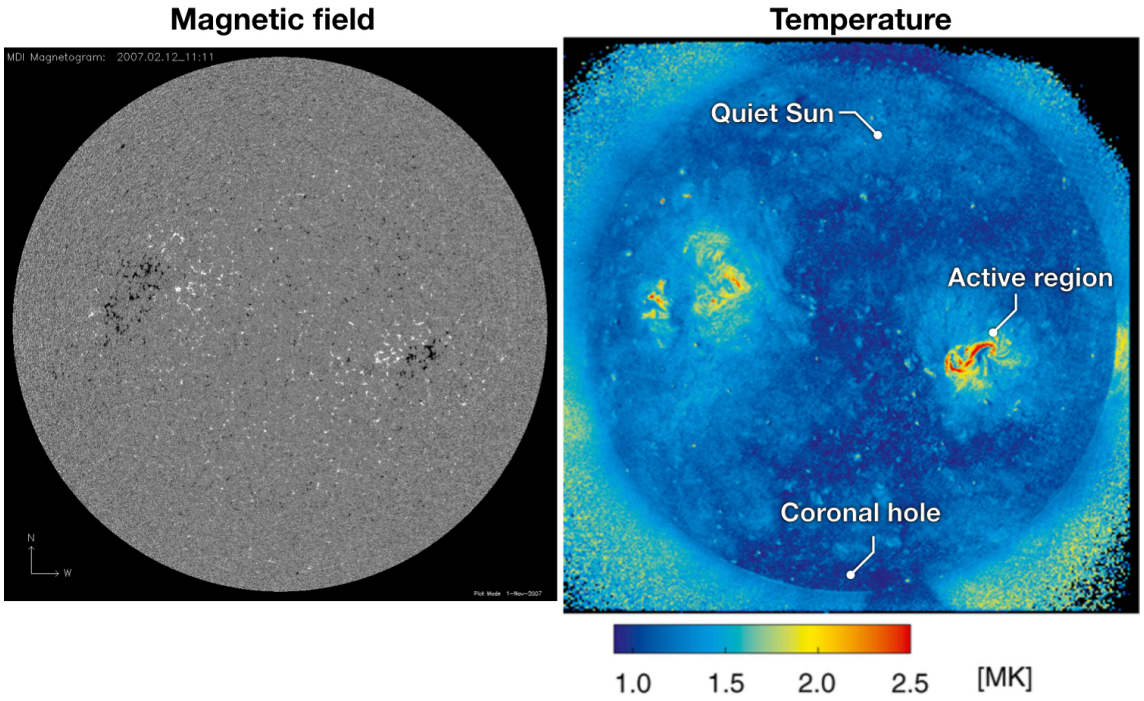

Figure 1.2: (Left) Photospheric magnetic field. White is the positive polarity and black is the negative polarity. The whiter and darker the color, respectively, the stronger the magnetic field strength. (Right) Coronal temperature obtained by the X-ray telescope onboard *Hinode* satellite (Kosugi et al., 2007) on the same day as the left panel observed by Narukage et al. (2011). It can be seen that the temperature of the corona is high in the region where the magnetic field is strong (i.e., active region).

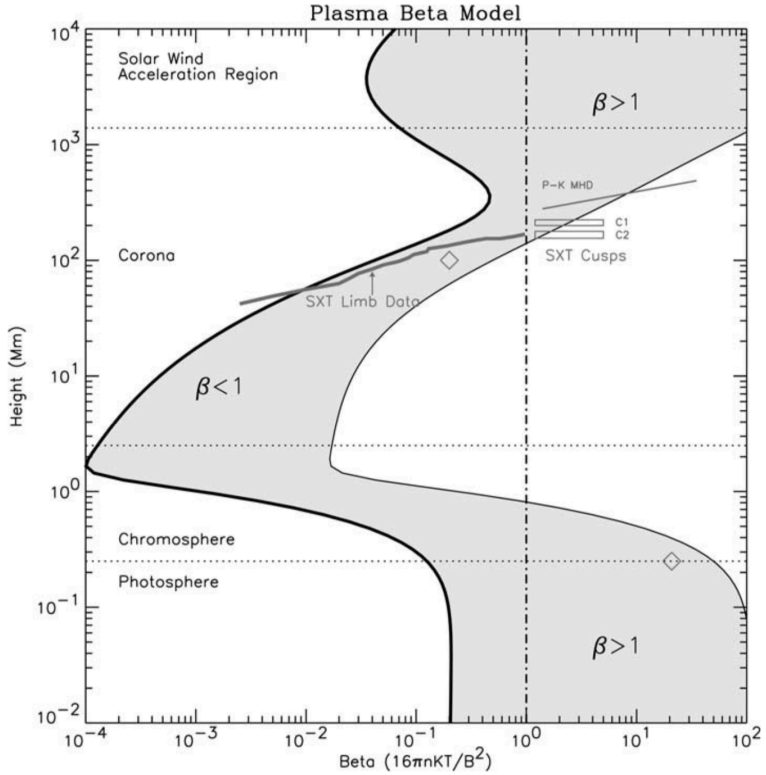

Figure 1.3: Plasma-β (gray shadow area) model on the solar atmosphere as a function of height in an active region. Thick line and thin line indicate a sunspot (2500 G) and a plage region (150 G), respectively. Figure adapted from Gary (2001).

1.2.2 Micro-flare heating

In the Sun, an explosive phenomenon called flare occurs. The energy release of this flare is considered to be due to magnetic energy converting into thermal and kinetic energy through magnetic reconnection. The energy released by a large flare ranges from 10^{29} to 10^{32} erg. In contrast, flares with an energy of 10^{26} erg or less are called micro-flares. However, if there are many micro-flares, then they add up and the sum of the energy released by them is comparable to the energy released by a large flare. For a small-scale contribution to the coronal heating, calculations suggest that the power-law index α of the relationship between flare energy and scale should be 2 or larger (Hudson, 1991), similar

to the following equation, where W is the total flare energy, and N is the frequency.

$$\frac{dN}{dW} \sim W^{-\alpha} \tag{1.1}$$

According to the results of soft X-ray observations of the *Yohkoh* satellite (Tsuneta et al., 1991), α is reported to be 2 or less in the energy power range of 10^{27}–10^{29} erg (Figure 1.4; Shimizu 1995; Aschwanden et al. 2000). If the micro-flares contribute to heating, the distribution at lower energies ($W < 10^{27}$ erg) should be different and steeper (i.e., $\alpha > 2$). Hence, studies using highly sensitive X-ray detectors are regarded as important. Since magnetic reconnection occurs in the closed magnetic region, micro-flare heating is important for magnetically active and flaring regions, but not for the quiet, magnetically inactive region.

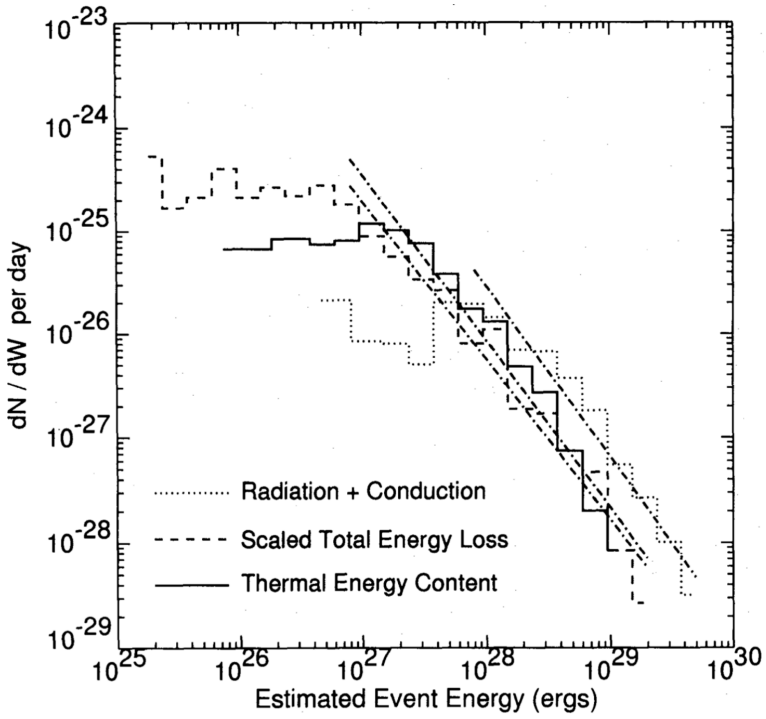

Figure 1.4: Power-law distribution of solar flare in the energy range of 10^{27}–10^{29} erg. Figure adapted from Shimizu (1995).

1.2.3 Wave heating

The surface of the Sun is in a turbulent state owing to convective motions and waves constantly being generated (Vögler et al., 2005; Kato et al., 2011, 2016). Some of these waves propagate to the corona and dissipate their energy, which can contribute to the heating of the corona (Figure 1.5). For example, surface convection sways the magnetic field lines that propagate Alfvén waves, which are magnetohydrodynamic (MHD) waves that propagate along the magnetic field line.

Since the plasma density decreases with height above the solar surface, the amplitude of a compressible wave such as a sound wave amplifies as it propagates upward and becomes a shock wave. As such, compressible waves are considered to be damped quickly and unable to transport sufficient energy to the corona. In contrast, an incompressible wave such as an Alfvén wave is less likely to dissipate than compressible waves and is considered a good candidate for the efficient energy transport mechanism. The incompressible wave also dissipates as a compressible wave by mode conversion, which occurs around a plasma-$\beta = 1$ layer (Hollweg et al., 1982). In addition, these waves are reflected around discontinuous plasma densities and magnetic fields, which can cause turbulence and dissipate energy when upward and downward waves collide (Matthaeus et al., 1999). Matsumoto & Suzuki (2014) reported that the chromosphere could be heated by compressible waves such as shock waves and that the lower part of the corona can be heated by an incompressible wave process based on their MHD simulation.

A direct observation of wave propagation in the corona was conducted using the Coronal Multi-channel Polarimeter (CoMP) with a coronagraph (Tomczyk et al., 2007; Tomczyk & McIntosh, 2009). However, the velocity amplitude obtained by this observation was as small as $1\ \mathrm{km\ s^{-1}}$, and the observed energy flux ($10\ \mathrm{erg\ cm^{-2}\ s^{-1}}$) of the waves was insufficient for heating the quiet corona (Table 1.1). The reason the observed velocity amplitude was small might be that the Doppler velocity was suppressed owing to the superpositions of waves along the line-of-sight. In fact, a relatively wide emission line

width was observed, which may have been caused by superpositions of various velocity components along the line-of-sight. Studies have been conducted to estimate the wave damping (Hahn et al., 2012; Hahn & Savin, 2013), assuming that the broadening of the emission line width was due to the superposition of various velocity components along the line-of-sight without considering the spatial distribution. In these studies, it was found that the observed emission line width decreased from what was expected, assuming that the energy was conserved as it propagated upward. This is considered to be evidence that wave energy is damped in the corona. However, more rigorous evaluations are required, as the waves were not spatially resolved.

To estimate the energy transported to the corona, it is necessary to resolve waves. Okamoto et al. (2007) reported waves traveling in a prominence, which is a low-temperature plasma blob of about 10^4 K floating in a corona of 10^6 K. The transported energy is quantitatively sufficient to heat the corona. In addition, Okamoto et al. (2015) and Antolin et al. (2015) reported evidence of a heating process associated with waves by comparing the different temperature structures using observational data and numerical results. However, as the prominence only exists in a limited area in the solar atmosphere, this observation cannot explain the heating of the entire corona. Therefore, in this study, to pay attention to the universality of the heating mechanism, we focus on jet-like structures called spicules that exist everywhere in the chromosphere to understand the energy transportation process.

The energy attributed to the heating of the corona passes through the chromosphere before reaching the corona. In the chromosphere, there is a spicule extending toward the corona, and its structure can be used to evaluate the energy flux toward the corona. In the next section, we will discuss the characteristics of and previous studies on the spicule, which will also be the focus of this study.

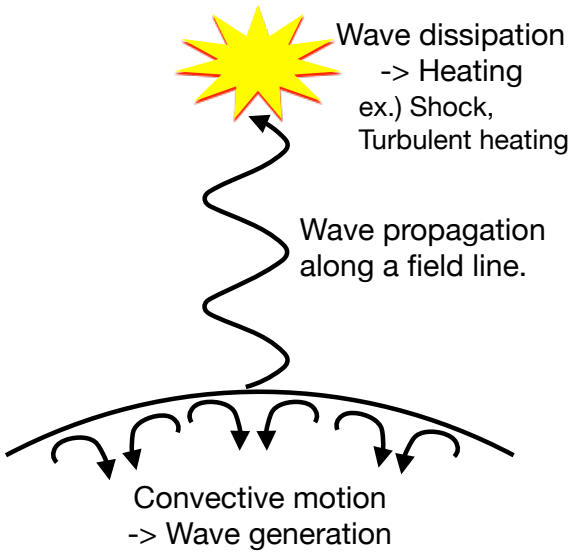

Figure 1.5: Schematic view of wave generation, transportation, and dissipation processes.

1.3 Spicule

1.3.1 Overview

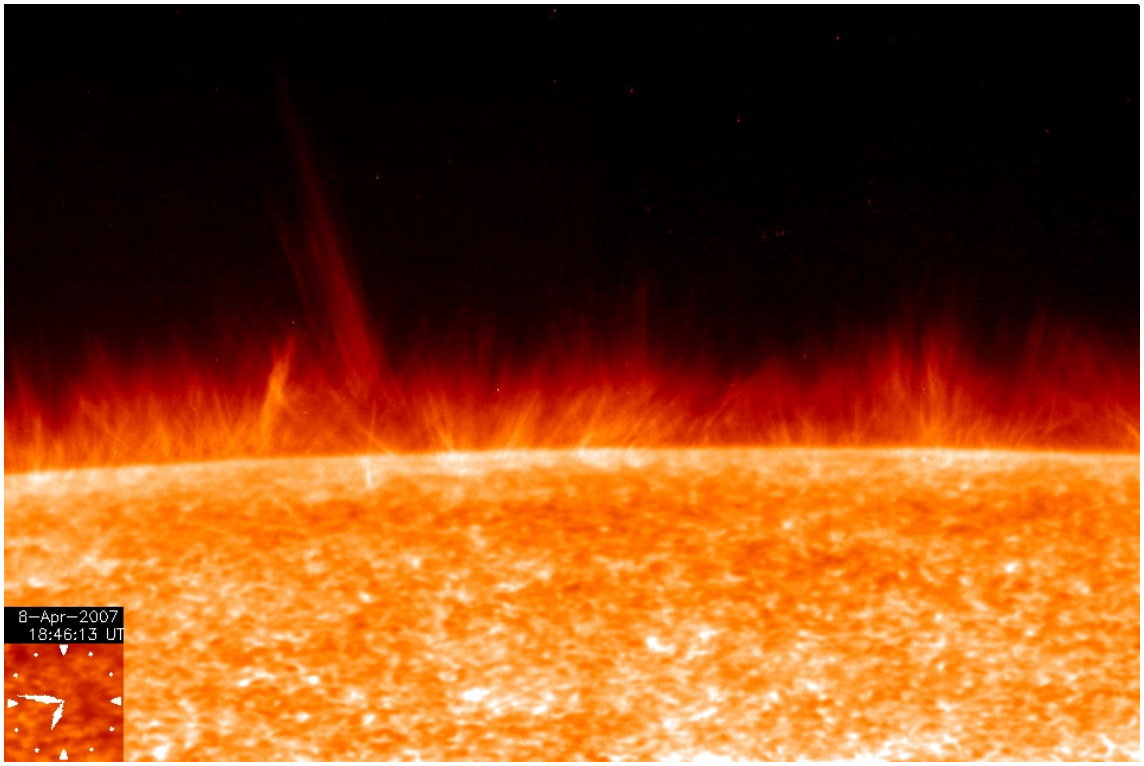

Figure 1.6: Spicules seen in off-limb region observed by *Hinode*/Solar Optical Telescope (SOT; Tsuneta et al. 2008; Suematsu et al. 2008) Ca II H line filter. Courtesy of NAOJ/JAXA and Joten Okamoto.

As shown in Figure 1.6, spicules are jet-like structures that can be clearly observed in the off-limb region of the solar chromosphere. Spicules were observed for the first time during a solar eclipse by Secchi (1875). On the solar disk, there are similar jet-like structures called mottles, which are considered to be on-disk counterparts of the off-limb spicules. We call them chromospheric jet-like structures in this thesis, without distinguishing names. Off-limb spicules enable us to observe their elongated structure from the side and investigate the height variation of spicules with time. Figure 1.7 shows examples of off-limb spicules captured by recent high-spatial and temporal observations with

multi-temperature coverage. After the appearance of the spicules, their length changes with time as a parabolic function (e.g., bottom left panel of Figure 1.7). The rising speed is about 10–60 $\mathrm{km\ s^{-1}}$ (Tsiropoula et al., 2012). The spicule height often extends to about 10 Mm, but some reach about 20 Mm (Alissandrakis et al., 2005). If the time range from the start of the parabolic movement to the end is defined as the lifetime of a spicule, it is about 2–12 min (Tsiropoula et al., 2012). After the spicule's disappearance, the heating process associated with the spicule's evolution is considered by tracing different temperature structures (Figure 1.7). As shown in the Figure 1.7 of the Ca II H line image (formation temperature is about 9×10^3 K) and the Si IV line image (formation temperature is about 8×10^4 K), the spicule appears in the Si IV line image after its disappearance in the Ca II H line image. This indicates that a spicule is heated at least to the transition region temperature of about 10^5 K.

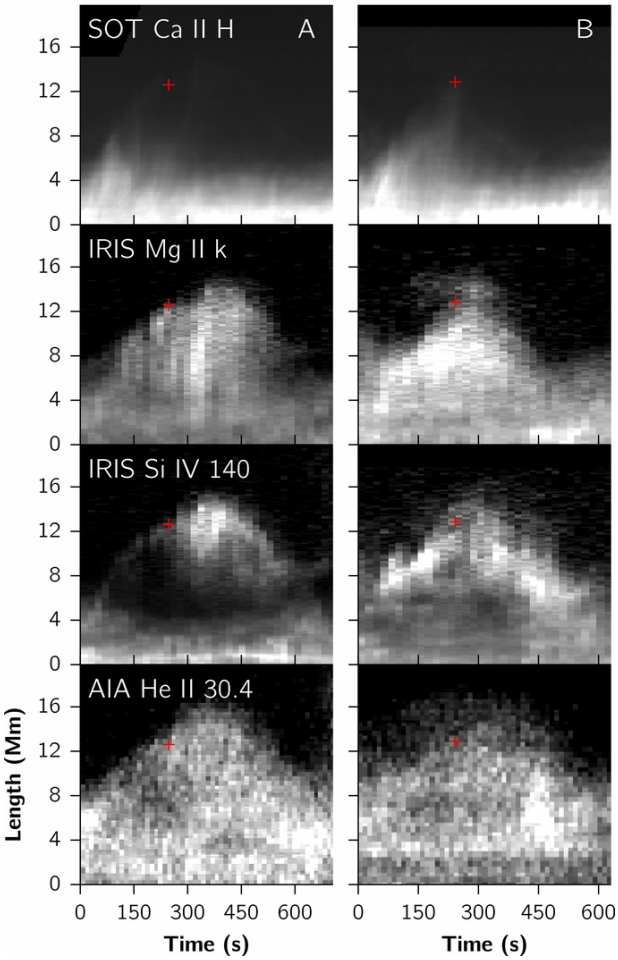

Figure 1.7: Temporal evolution of spicule height simultaneously observed by *Hinode*/SOT, the Interface Region Imaging Spectrograph (IRIS; De Pontieu et al. 2014) and the Solar Dynamics Observatory/Atmospheric Imaging Assembly (SDO/AIA; Pesnell et al. 2012; Lemen et al. 2012). From the top, filter images of the Ca II H line (396.9 nm), the Mg II k line (279.6 nm), the Si IV line (139.4 & 140.3 nm), and the He II line (30.4 nm). The formation temperature of each spectral line is about 9×10^3 K, 1×10^4 K, 8×10^4 K, and 1×10^5 K from the top. It can be seen that over time, spicules are starting to appear with high formation temperatures. Figure adapted from Pereira et al. (2014).

From observations of the solar disk, spicules are considered to be rooted in the super-

granular boundaries where the kG vertical magnetic fields, so-called network fields, are advected by the horizontal convective flow (Samanta et al. 2019 and Figure 1.8). As shown in the left panel of Figure 1.8, spicules (black jet-like structures) are concentrated around a kG magnetic field (blue patches) around the super-granular boundaries. In addition, as shown in the right panel of Figure 1.8, dipole magnetic fields have been found at the base of spicules in recent observations with high spatial resolution. It could be confirmed from the temporal variation of spicules and photosphere magnetic fields that a bipolar magnetic field becomes a monopolar magnetic field at the same time as a spicule generation happens, or a monopolar magnetic field becomes a bipolar magnetic field at the same time as spicule generation happens. Both processes of spicule formation are considered to be the result of the magnetic reconnection, but the reconnection pair is different. In the first case, the magnetic reconnection happens in the pre-existing bipolar magnetic field. The latter's magnetic reconnection happens between the pre-existing monopolar magnetic field and an emerging (newly appearing) bipolar magnetic field. This suggests that the magnetic field plays an important role in the dynamics of spicules.

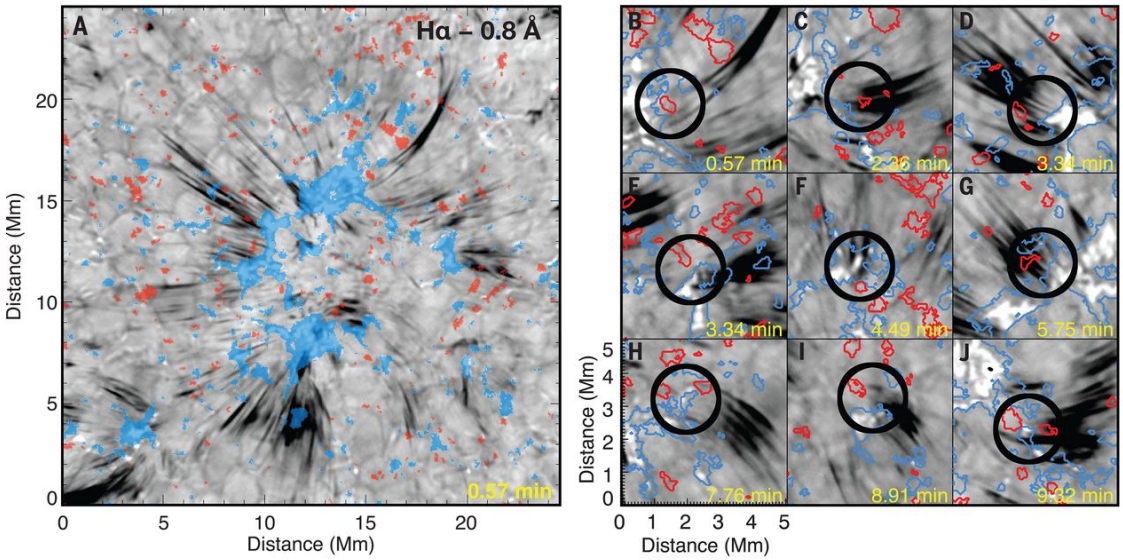

Figure 1.8: (Left) H$\alpha-0.8$ Å filter image. Structures on the photosphere, such as granules are mainly visible, but structures moving in the line-of-sight direction, such as spicules (black jet-like structures), can also be observed at the same time. The red and blue patches represent photospheric magnetic field strengths stronger than $+10$ G and weaker than -10 G, respectively. (Right) Enlarged view of the spicules and their roots (black circle). The red and blue contours represent positive and negative magnetic polarities, respectively. Figure adapted from Samanta et al. (2019).

From this observation, we can imagine the view of the spicules, magnetic field, and convections similar to Figure 1.9. However, as the structure of the spicule's magnetic field has not been well studied yet, it is not clear whether it actually has this structure.

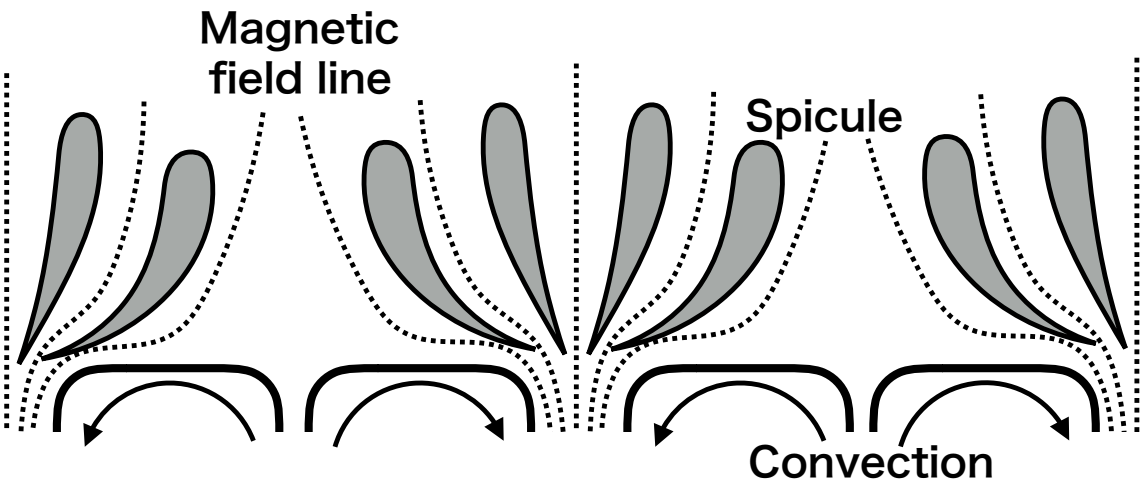

Figure 1.9: Schematic view of the spicules, magnetic field, and convections.

1.3.2 Oscillation

The high-resolution observations by *Hinode*/Solar Optical Telescope (SOT) revealed oscillations along the spicule (Figure 1.10; De Pontieu et al. 2007; He et al. 2009; Okamoto & De Pontieu 2011). The magnetic fields are frozen into the plasma. Therefore, the oscillations of the spicules can be inferred to be the oscillations of the magnetic fields, and they propagate as Alfvén waves. The observed oscillations are classified into two categories: one with a long period in the order of minutes, and the other with a short period in the order of seconds. In particular, oscillations with a period of several tens of seconds have a shorter oscillation wavelength than a spicule's length, so that the propagation of waves along the spicules can be identified. Okamoto & De Pontieu (2011) automatically detected spicule oscillations from imaging data obtained by the *Hinode* and found propagation of waves with a period of about 40 s. From this observation, it was found that there are not only waves propagating upward, but also propagating downward, which are reflected at the top of the chromosphere. Long-period oscillations have a longer oscillation wavelength than a spicule's length, making it difficult to observe the propagation of waves only by observing spicules (De Pontieu et al., 2007). Long-period wave propagations have

been found in the coronal loop (Tomczyk et al., 2007; Tomczyk & McIntosh, 2009) and they are considered to be related to the long-period oscillations found in spicules (McIntosh et al., 2011). In this way, spicules, which are observed everywhere on the solar chromosphere, can be the energy path connecting the photosphere and the corona, and are therefore regarded as important in considering the mechanism of the universal heating of the corona.

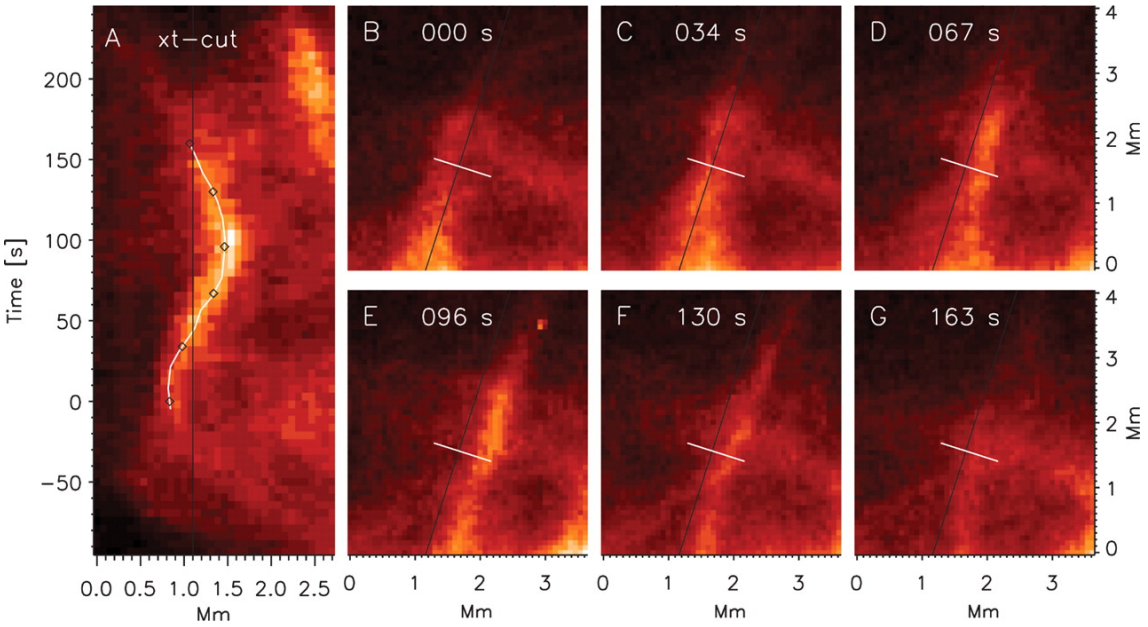

Figure 1.10: The example of the long-period oscillation. (Panel B–G) Snapshots of spicule oscillation perpendicular to its axis. (Panel A) Space time plot along the white line shown in panel B–G. Figure adapted from De Pontieu et al. (2007).

In the case of a transverse wave such as the Alfvén waves, the energy flux F can be written as the following equation.

$$F = \frac{1}{2}\rho v_a^2 v_p \tag{1.2}$$

Here, ρ is the density of the spicule, v_a is the velocity amplitude, and v_p is the wave propagation velocity. Short-period waves found by Okamoto & De Pontieu (2011) have a velocity amplitude of approximately 7 $\mathrm{km\ s^{-1}}$ and a propagation velocity of approxi-

mately $270\ \mathrm{km\ s^{-1}}$. By assuming a spicule number density of $10^{10}\ \mathrm{cm^{-3}}$ from a previous study (Beckers, 1968), the energy flux was estimated to be $2.5 \times 10^5\ \mathrm{erg\ cm^{-2}\ s^{-1}}$. If we consider the filling factor of the spicules in the chromosphere, it can be seen that this is insufficient to heat the corona in the quiet region. However, the energy estimation may not be accurate because the velocity amplitude, which is important for estimating the energy, is obtained only from the apparent amplitude by using imaging data. Moreover, the density is assumed based on a previous study. To quantitatively determine the transport energy to the corona, it is important to directly derive the velocity amplitude from spectroscopic observations.

Determining the magnetic field is also important for estimating the amount of energy transported to the corona. Assuming the wave transported to the corona to be an Alfvén wave, the wave propagation velocity can be expressed by the following equation.

$$v_p = \frac{B}{\sqrt{4\pi\rho}}, \tag{1.3}$$

where B is the magnetic field strength. Combining this Equations (1.2) and (1.3), the energy flux is expressed by

$$F = \frac{B^2 v_a^2}{8\pi v_p}. \tag{1.4}$$

Using this formula, the energy flux can be estimated directly from observing the magnetic field strength, wave propagation velocity, and velocity amplitude (i.e., without assuming a density from previous studies).

1.3.3 Magnetic field

Spicules and magnetic fields are considered to have an important relationship, as described in Section 1.3.1. The spicule's magnetic field is measured mainly by inferring the polarization spectra obtained by spectro-polarimetric observation (see Section 1.5).

Trujillo Bueno et al. (2005) succeeded in measuring these magnetic fields for the first time with the He I triplet lines at $1083.0\ \mathrm{nm}$ with a ground-based telescope and reported that their field strength is at least 10 G. From other observations with He I triplet lines, a magnetic field strength of about 10–80 G (Centeno et al., 2010; Orozco Suárez et al., 2015) is obtained. López Ariste & Casini (2005) compared the structures of the spicules with the inclination of the magnetic field using the He I D_3 line ($587.6\ \mathrm{nm}$) and reported that the spicules align with the magnetic field lines (Figure 1.11). Orozco Suárez et al. (2015) investigated a height variation of the magnetic structure along the spicules (Figure 1.12) and found that a spicule's magnetic fields weakens from about 80 G to 10 G from the bottom to the top of the spicule (left panel of Figure 1.12).

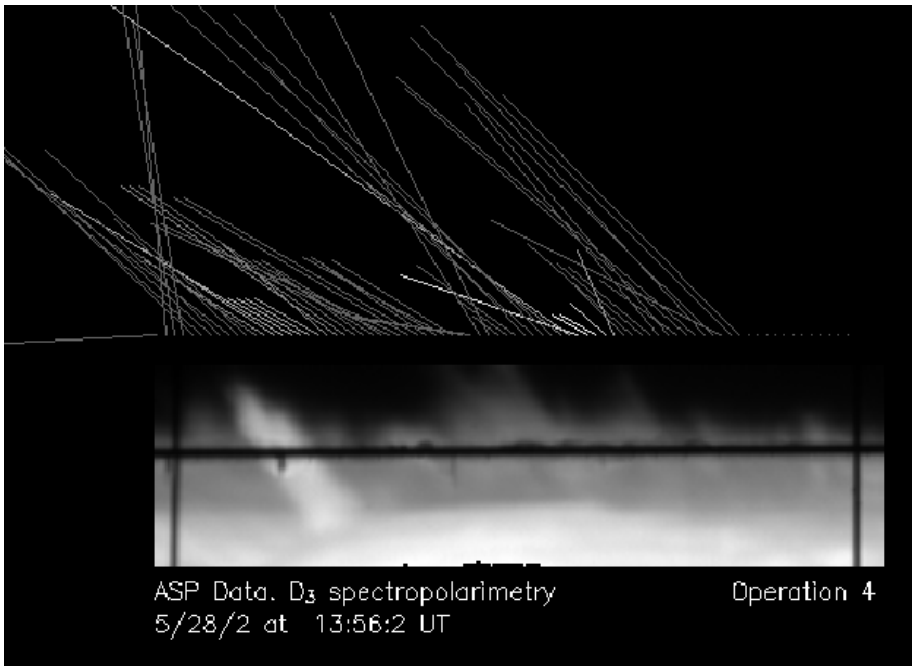

Figure 1.11: (Bottom) Hα line filter image. The horizontal black line represents the slit position. (Top) The inclination and strength of the magnetic field at the slit position obtained by using the He I D_3 line ($587.6\ \mathrm{nm}$). The direction of the line is the inclination, and the length represents the strength. Figure adapted from López Ariste & Casini (2005).

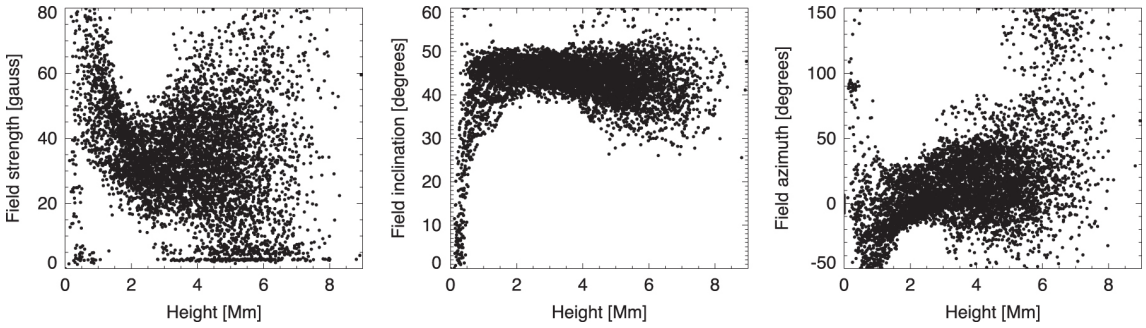

Figure 1.12: From left to right, magnetic field strength, inclination, and azimuth as a function of height from visible solar surface. Figure adapted from Orozco Suárez et al. (2015).

In addition to the spectro-polarimetric observation, there is another method of obtaining magnetic field strengths from the propagation velocity v_p of the waves in the spicules, by using the relation of Equation (1.3), and assuming the spicule density. The magnetic field strengths of spicules are estimated to be 10–80 G (Singh & Dwivedi, 2007; Zaqarashvili et al., 2007; Kim et al., 2008). These inferred field strengths are similar to the results obtained by spectro-polarimetric observation.

1.4 The Lyα line

The height range from the upper chromosphere to the corona can be observed using ultraviolet wavelength due to its plasma temperature. The Lyα line (121.57 nm) is emitted from hydrogen, which is the most abundant element in the Sun, through the first excited blended two levels ($2p^2\mathrm{P}_{1/2}$ and $2p^2\mathrm{P}_{3/2}$) to the ground level ($1s^2\mathrm{S}_{1/2}$) and is an extremely bright emission line. The line core is generated around the bottom of the transition region and the line wing is generated around the top of the chromosphere (Vernazza et al., 1981). Therefore, the Lyα line is useful for investigating the influences of the height range, from with the possibility of the observation of high temporal resolution data due to its brightness.

From the point of view of magnetic field measurements, the Lyα line has a short wavelength and a wide line width due to thermal motion, and therefore its sensitivity to the Zeeman effect is small (for more detail, see Section 1.5.1). On the other hand, based on numerical results (Štěpán & Trujillo Bueno, 2011; Trujillo Bueno et al., 2011; Belluzzi et al., 2012), the Lyα line core has a sensitivity to the Hanle effect and $B_{\rm H} = 50$ G (from Equation 1.7 with $g = 4/3$, and $t_{\rm life} = 1/6.27 \times 10^{-8}$ s), so it is sensitive to a magnetic field strength of 10 G to 250 G (for more detail, see Section 1.5.2). Figure 1.13 shows the change in polarization degree (Stokes Q) when the magnetic field strength is changed. From this figure, it can be seen that if the spectro-polarimeter can observe it with an accuracy of 0.1% or more, the magnetic field can be quantitatively derived.

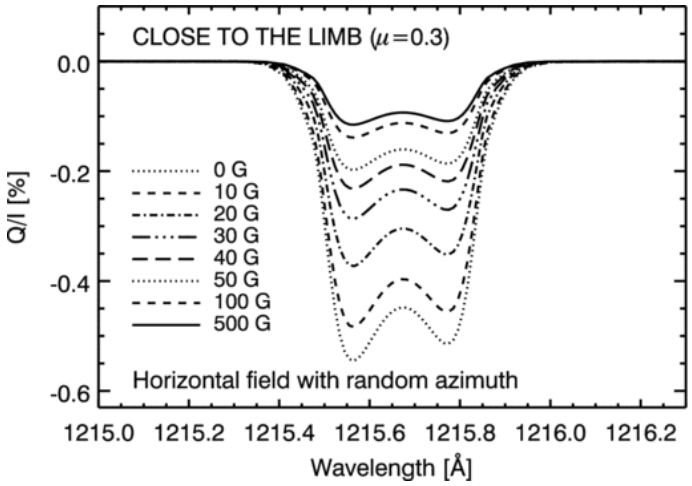

Figure 1.13: Stokes Q profile with respect to the magnetic field strength at close to the limb observation. Figure adapted from Trujillo Bueno et al. (2011).

As ultraviolet lines are absorbed by the Earth's atmosphere, they need to be observed outside the Earth's atmosphere. The observations of the rocket experiment Very high Angular resolution ULtraviolet Telescope (VAULT; Vourlidas et al. 2010) with a high spatial resolution in the Lyα line (0.49 arcsec) found that average structures of about 1 arcsec are distributed in the chromosphere.

1.5 Magnetic Field Measurement

1.5.1 Zeeman effect

The solar magnetic field is mainly measured using the Zeeman effect. In the presence of a magnetic field, the atomic energy level of the total angular momentum J splits into $(2J+1)$ magnetic sub-levels, which are characterized by the magnetic quantum number M. Only transitions with $\Delta M = 0$ and ± 1 are allowed and each component of the light (σ components with $\Delta M = \pm\pi$ and components with $\Delta M = 0$) is polarized depending on the geometry between the direction of the magnetic field and the observer. The Zeeman splitting $\Delta\lambda_B$ (i.e., wavelength displacement of σ components) is defined as in the following equation.

$$\Delta\lambda_B = 4.67 \times 10^{-13} \lambda^2 g_{\rm eff} B, \tag{1.5}$$

where λ is a wavelength of spectral line, $g_{\rm eff}$ is an effective Landé factor of the transition, and B is a magnetic field strength (in Gauss).

The Zeeman effect is a powerful diagnostic tool for photospheric magnetic fields. The SOT aboard the *Hinode* satellite, which started its observation in 2006, has enabled high spatial resolution and high precision spectro-polarimetric observation at the Fe I 630.15 nm and 630.25 nm lines for the first time and revealed the photospheric magnetic fields in greater detail (e.g., Lites et al. 2008; Ishikawa & Tsuneta 2009). In the weak field regime, the circular polarization induced by the Zeeman effect is proportional to $\Delta\lambda_B/\Delta\lambda_D$, while the linear polarization is proportional to the square of $\Delta\lambda_B/\Delta\lambda_D$ (Trujillo Bueno et al., 2017). Note that $\Delta\lambda_D$ is the Doppler broadening and is given by

$$\Delta\lambda_D = \frac{\lambda}{c}\sqrt{\frac{2k_{\rm B}T}{M}}, \tag{1.6}$$

where $k_{\rm B}$ is Boltzmann's constant, T is a formation temperature of spectral line, c is

the light speed, and M is the mass of the element. In the chromosphere, the magnetic field is weaker than in the photosphere, and the spectral lines show a larger Doppler broadening due to the higher temperature and/or non-thermal velocities. Therefore, in the chromosphere, the polarization signals induced by the Zeeman effect are excessively small to be detected except in the active regions.

Instead, the Hanle effect, whose polarization signal is not affected by Doppler broadening and can be sensitive to weaker magnetic fields, has been focused on in recent years (Trujillo Bueno et al., 2011).

1.5.2 Scattering polarization and Hanle effect

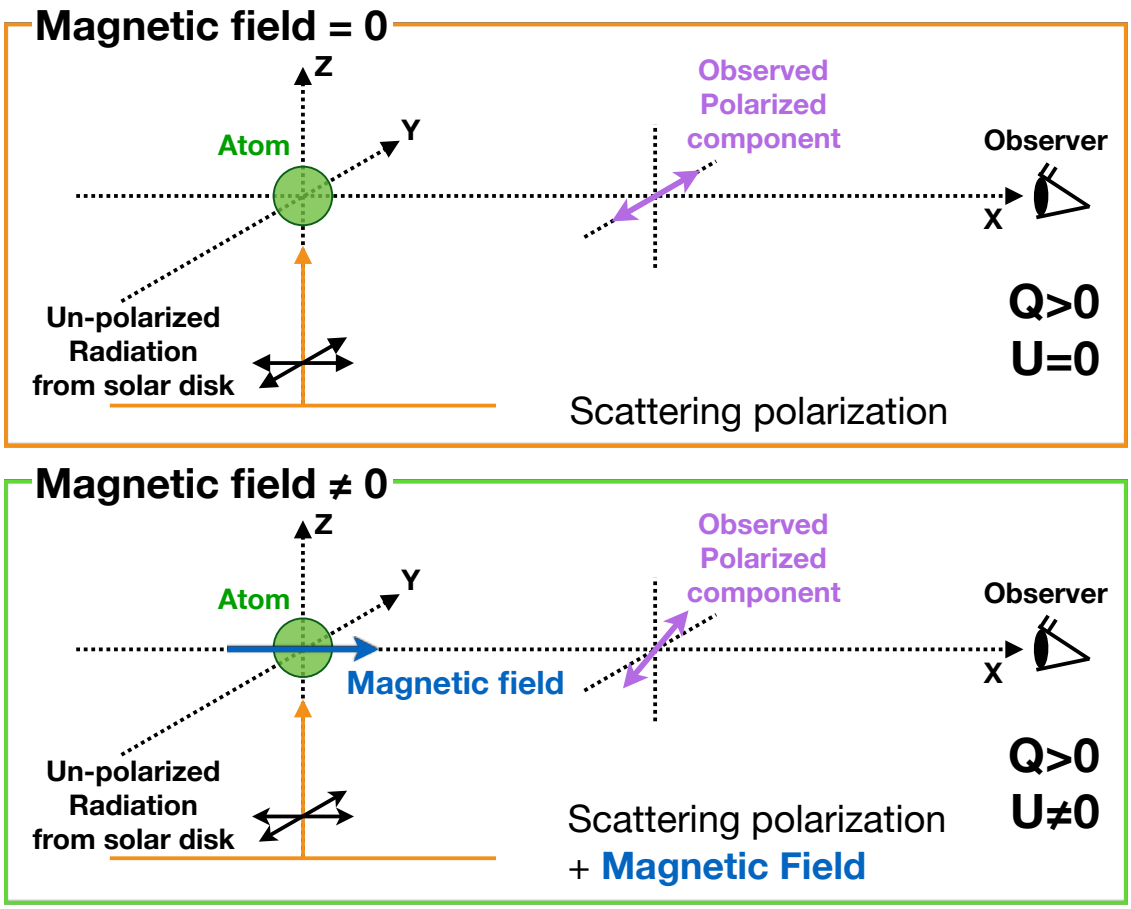

Figure 1.14: Schematic views of the effect of scattering polarization (top panel) and the Hanle effect (bottom panel) in the case of off-limb observation (i.e., line-of-sight is parallel to the X-axis).

As the magnetic field of the chromosphere is weak, it is effective to use the Hanle effect to investigate the magnetic field of the solar atmosphere. The Hanle effect describes how the magnetic field modifies the polarization states induced when the atom scatters in the anisotropic radiation field. Here, we consider an atom located above the limb and illuminated by the un-polarized radiation from below (i.e., 90° scattering, top panel of Figure 1.14). The illuminating radiation is axisymmetric but not isotropic. Now, the polarization in the direction parallel to the solar limb is defined as the Stokes $+Q$, and

in the vertical direction as $-Q$. The positive and negative Stokes U is defined as being rotated 45° counterclockwise from the Stokes Q.

We explain the classical view of the scattering polarization and the Hanle effect in the following Section 5.13 of Landi Degl'Innocenti & Landolfi 2004. (i) The incident radiation has an electric field with an X-component and a Y-component. (ii) They excite atoms with an X-component oscillation and a Y-component oscillation. (iii) With the decay of each oscillation, a dipole radiation polarized in the oscillation direction is generated. As dipole radiation does not propagate in the oscillation direction, the radiation derived only from oscillation in the Y-component is observed as scattering polarization in the Y direction. Hence, the scattering polarization is polarized in the $+Q$ direction and $U = 0$.

In the presence of a magnetic field, an atom's oscillation precesses around the magnetic field direction (Larmor precession) with a Larmor frequency $\nu_{\rm L}$ that is proportional to the magnetic field strength. The de-excitation occurs on the time scale of spontaneous emission, as determined by Einstein's A-coefficient. If the de-excitation time scale $t_{\rm life}$ (reciprocal of Einstein's A-coefficient) is comparable to the period of the Larmor precession ($t_{\rm life} \sim 2\pi\nu_{\rm L}^{-1}$), the scattering polarization is decreased and rotated. [1] As a result, the observed Q and U signals change from the ones where the magnetic field is zero (bottom panel of Figure 1.14). The critical Hanle field strength $B_{\rm H}$ (in Gauss) is defined by

$$B_{\rm H} = \frac{1.137 \times 10^{-7}}{t_{\rm life} g}, \tag{1.7}$$

where g is a Landé factor (Trujillo Bueno et al., 2011). The linear polarization is sensitive to the field strength due to the Hanle effect approximately from $0.2B_{\rm H}$ to $5B_{\rm H}$.

The case considered in Figure 1.14, in which the radiation comes only from below in the vertical direction is extreme. To evaluate the scattering polarization quantitatively, it is necessary to consider the stratification of the solar atmosphere. The radiation field is described by the radiation field tensors J^K_L (K and L are integer with $K \geq |L|$) (Eq.

[1] If the $t_{\rm life}$ is much longer than the period of the Larmor precession ($t_{\rm life} \gg 2\pi\nu_{\rm L}^{-1}$), the scattered light is totally unpolarized. In this case, the magnetic field is strong and is called the Hanle satulated regime.

(5.157) of Landi Degl'Innocenti & Landolfi 2004). Especially, the imbalance between the vertical radiation and the horizontal radiation is quantified by J^2_0/J^0_0. For example, in Figure 1.15, the atom is located at an optical thickness $\tau \gg 1$, the atom is illuminated from all directions, and J^2_0/J^0_0 is 0. In contrast, if τ is smaller than unity, the atom is mainly illuminated from the below and the illumination from the vertical direction dominates (i.e., $J^2_0/J^0_0 > 0$). The J^2_0/J^0_0 is proportional to the Stokes Q/I in the absence of a magnetic field (Trujillo Bueno et al., 2011).

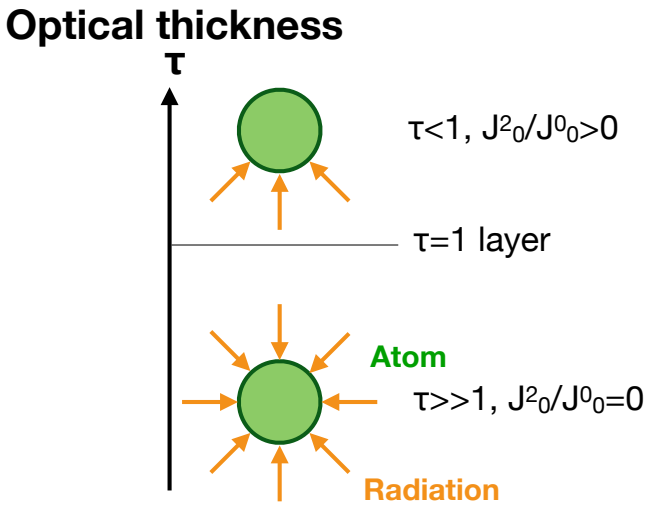

Figure 1.15: Schematic picture of radiation illuminating atom and anisotropy J^2_0/J^0_0 with height (optical thickness).

1.6 CLASP Sounding Rocket Experiment

1.6.1 Overview

The Chromospheric Lyman-Alpha Spectro-Polarimeter (CLASP; Kano et al. 2012; Kobayashi et al. 2012) is a sounding rocket experiment aimed at opening up a new diagnostic window into exploring the magnetic fields of the upper chromosphere and the transition region using the Hanle effect. It was launched on September 3, 2015 and succeeded in

spectro-polarimetric observations with high accuracy with a precision of 0.1% in the vacuum ultraviolet (VUV) range for the first time (Giono et al., 2016b, 2017). It detected the scattering polarization in the hydrogen Lyα line (Kano et al., 2017) and Si III line at 120.65 nm (Ishikawa et al., 2017a), in addition to the Hanle effect in these UV spectral lines (Ishikawa et al., 2017a). Although the observing target of CLASP was the quiet Sun near the limb to maximize the possibility of detecting scattering polarization, CLASP fortunately captured the initial phase of the evolution of an off-limb spicule. CLASP is also a high throughput "spectrometer" and provided us with the Lyα intensity spectra with an unprecedentedly high temporal cadence of 0.3 s. In this thesis, we used these valuable data sets to investigate the dynamics and magnetic fields of a spicule.

1.6.2 CLASP instrument

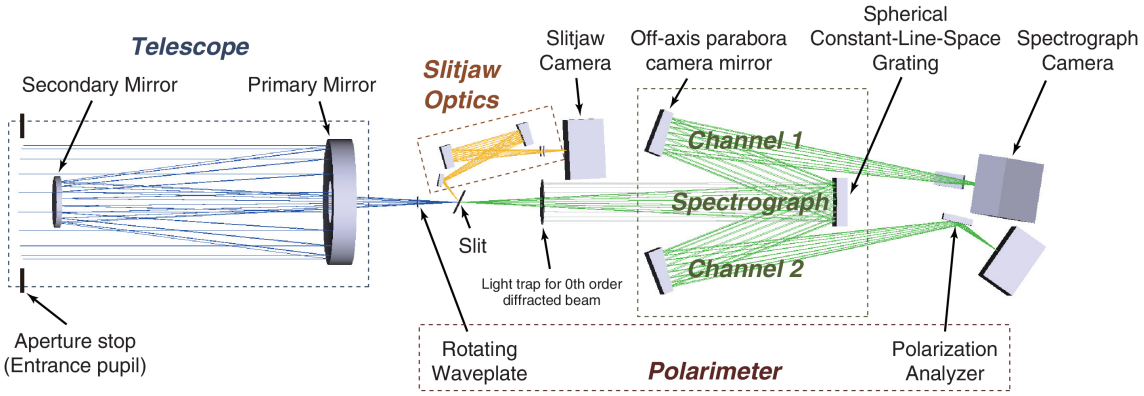

Figure 1.16: Optical design of CLASP instrument. Figure adapted from Narukage et al. (2015).

The CLASP instrument is composed of a Cassegrain telescope, a Slitjaw Imager (SJ), and a Spectro-polarimeter (SP), as shown in Figure 1.16. The number of optical components was minimized (Narukage et al., 2015) and high-reflectivity coatings were applied to all reflective mirrors (Narukage et al., 2017) to achieve a high throughput (i.e., the high precision) in VUV. For the wavelength selection, the primary mirror of the telescope uses a cold-mirror coating targeting 121.57 nm. The cold-mirror coating is a narrowband mul-

Table 1.2: CLASP SJ and SP overview (see also Narukage et al. 2015; Giono et al. 2016a) (1 arcsec $\approx$ 730 km on the Sun)

Slit-Jaw (SJ)	
Field of view	527 arcsec $\times$ 527 arcsec
Spatial sampling	1.03 arcsec/pixel
Spatial resolution	3 arcsec
Spectral coverage (Band width)	121.57 nm with 7 nm FWHM
Temporal cadence	0.6 s
Spectro-Polarimeter (SP)	
Field of view along slit	400 arcsec
Slit width	1.45 arcsec
Spatial sampling	1.11 arcsec/pixel
Spatial resolution	3 arcsec
Spectral sampling	0.0048 nm/pixel
Spectral resolution	0.01 nm
Spectral coverage	121.567 ± 0.61 nm
Temporal cadence	0.3 s
Temporal cadence of polarization	1.2 s
Polarization accuracy	0.1%

tilayer coating that reflects the targeted wavelength but is transparent to visible light and plays an important role in decreasing visible light contamination for subsequent optical components (Narukage et al., 2017). The SJ is the Lyα imaging system to get the context chromospheric image around the slit for the co-alignment with other instruments. The SJ images were used to adjust and confirm the targeting during flight. Hence, the temporal cadence was as high as 0.6 s. The light passes through the slit and enters the SP section. The SP has the two optically symmetric channels that obtained two orthogonal polarization components simultaneously by rotating the reflective polarization analyzers by 90° with respect to each other (Narukage et al. 2015; right part of Figure 1.16). This arrangement enables the suppression of spurious polarizations caused by intensity fluctuations related to the Sun and the pointing drift and jitter (del Toro Iniesta, 2003).

1.6.3 Spectro-polarimetric Observation

As shown in Figure 1.17, CLASP measured the linear polarization using a rotating wave-plate (Ishikawa et al., 2013, 2015) and a polarizer. First, using a wave-plate, the direction of polarization is changed to a specific direction. Then, only a specific polarization direction is reflected at a polarizer with a Brewster's angle. By rotating the wave-plate, the polarization direction changes. The rotation of the wave-plate is synchronized with the CCD camera system. While the wave-plate completes one rotation in 4.8 s, the CCD camera obtains 16 data sets at intervals of 0.3 s. As a result, D_{t1}, D_{t2}, ... with 0.3 s exposure shown in the bottom panel of Figure 1.17 are obtained. The SP obtained two orthogonal polarization components simultaneously with two cameras.

The Stokes vector I, Q, and U can be demodulated by Equations (1.8)–(1.10), where a is a modulation coefficient, and K is the throughput of this instrument. Each data set was taken in 0.3 s cadences, therefore the Stokes vector Q, and U were demodulated in 1.2 s cadences. In addition, if we focus on only the spectral data and no polarization data is required, we can use data with a 0.3 s temporal resolutions.

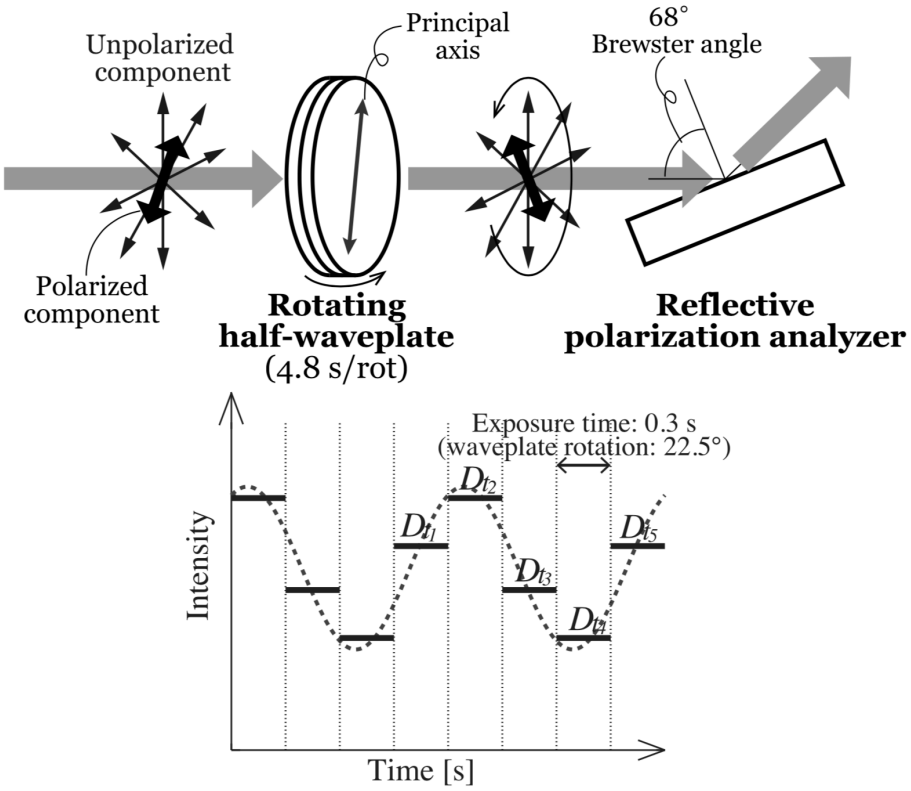

Figure 1.17: (Top) Schematic view of CLASP polarimeter consisting of a continuously rotating half-wave-plate and a reflective polarization analyzer. (Bottom) Example of the modulation curve for a partially linearly polarized beam (dotted line). Solid lines indicate the observed signal during each exposure. Figure adapted from Ishikawa et al. (2014).

$$I_1 = K(D_{t1} + D_{t2} + D_{t3} + D_{t4}) \tag{1.8}$$

$$Q_1 = aK(D_{t2} - D_{t3} - D_{t4} + D_{t5}) \tag{1.9}$$

$$U_1 = aK(D_{t1} - D_{t2} - D_{t3} + D_{t4}) \tag{1.10}$$

1.6.4 CLASP Observation

CLASP observed the disk center for polarization calibration in 14.4 s (Giono et al., 2017) and then observed the quiet Sun region near the limb to study the center-to-limb variation of the scattering polarization (Kano et al., 2017; Ishikawa et al., 2017a) in 277.2 s by positioning the slit perpendicular to the southwest limb. We identified the slit position using the full Sun observation taken by SDO/AIA He II 30.4 nm filter image, as shown in Figure 1.18. The spatial resolutions of SP and SJ are estimated to be 3 arcsec each (Giono et al., 2016a), by comparing with the AIA He II filter images, whose spatial resolution was estimated to be 1.2 arcsec (Lemen et al., 2012). The spectral resolution of SP is estimated to be 0.01 nm when compared with the width of the geo-coronal absorption line which came from the Earth's atmosphere and was obtained by the LPSP instrument onboard the OSO8 spacecraft, whose spectral resolution was estimated to be 0.002 nm (Gouttebroze et al., 1978).

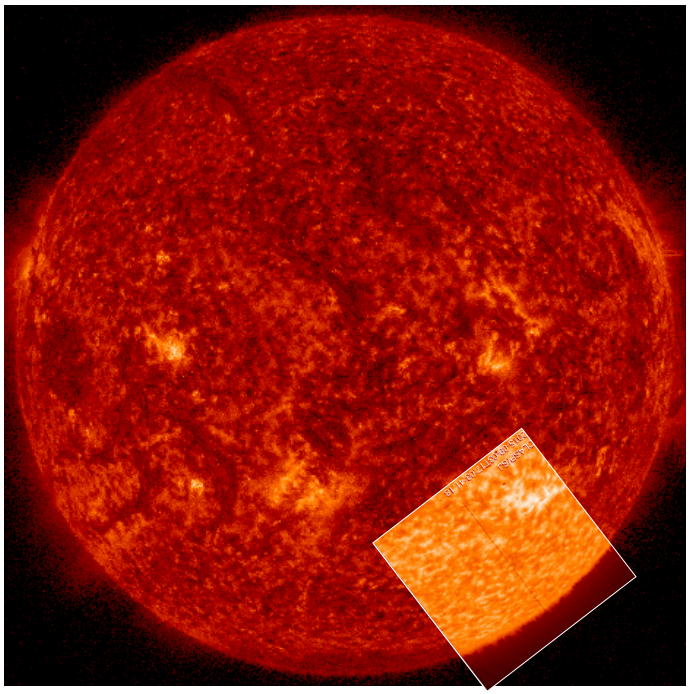

Figure 1.18: SDO/AIA He II $30.4\ \mathrm{nm}$ filter image (full Sun image with red color), and CLASP/SJ Lyα filter image (solar southwest part with orange color). The black line shown in SJ image corresponds to the slit position.

1.7 Aim of this Thesis

The solar atmosphere has a hot corona with a temperature of about $10^6\ \mathrm{K}$ above the photosphere, the temperature of which is about $5770\ \mathrm{K}$. Magnetic waves are considered to be a mechanism of energy transfer from the photosphere to the corona and partially responsible for the generation of the corona. However, previous coronal observations have not found sufficient wave energy for heating.

We focus on the chromosphere, the middle layer between the photosphere and the corona, to investigate whether there is a magnetic wave propagating upward into the chromosphere and whether it has sufficient energy to heat the corona. A characteristic structure of the chromosphere is a jet-like structure called spicule. Because spicules

are ubiquitous in the chromosphere, they are useful in investigating the universal mechanisms of heating in the corona. The CLASP sounding rocket experiment obtained spectro-polarimetric data of the spicule in the Lyα line with high temporal resolution and a high signal-to-noise ratio. We can expect that the magnetic field and velocity field ranging from the chromosphere to the transition region can be derived from the spectro-polarimetric data. By using spectroscopic data with unprecedented high temporal resolution, it is possible to investigate velocity fields that have not been clearly seen until now and phenomena that have never been seen in such detail, and that will contribute to understanding the dynamics of the chromosphere. This is a first and very challenging study with the aim of deriving a magnetic field in the ultraviolet wavelength range, which will provide new insights into the theoretical model, and will lead to observations by satellites in the future. In addition, the velocity field and magnetic field information obtained from these observational studies are important for estimating the amount of energy transported to the corona quantitatively, and for understanding the coronal heating mechanisms.

We discuss the velocity field of the spicule in Chapter 2 and the liner polarization which is important for the derivation of the magnetic field vector in Chapter 3. Finally, we summarize our study and discuss future prospects in Chapter 4.

Chapter 2

Wave Propagation along a Spicule[1]

2.1 Introduction

To maintain the solar corona at a temperature of around 10^6 K, magnetic energy needs to be transported from the photosphere. The chromosphere, which is the middle layer between the photosphere and corona, is thought to play an important role to transfer the energy for the coronal heating. In the chromosphere, vertically elongated structures called spicules are observed everywhere and it is of great interest to understand how these ubiquitous phenomena are relevant to the coronal heating.

In previous studies, two types of oscillation period (shorter than 2 minutes and longer than 2 minutes) had been observed in spicules (reviewed by Zaqarashvili & Erdélyi 2009). Long-period oscillations with periods of 2–8 minutes were found from the apparent motions of spicules using imaging observations (De Pontieu et al., 2007; McIntosh et al., 2011). These oscillations are considered to be magnetohydrodynamic (MHD) waves, which can transport sufficient energy to heat the quiet corona because of the large velocity amplitude. However, because the wavelengths of these long-period oscillations are longer than the typical spicule height (5–20 Mm; Alissandrakis et al. 2005; Teriaca et al. 2006; De Pontieu et al. 2007; Pasachoff et al. 2009), it remains uncertain whether such

[1]This chapter was published as Yoshida et al. 2019, "High-Frequency Wave Propagation Along a Spicule Observed by CLASP", Astrophysical Journal, 887, 2

oscillations propagate along spicules as a wave or not.

The wave propagation of short-period lateral oscillations (shorter than 2 minutes period) had been observed (He et al., 2009; Okamoto & De Pontieu, 2011; Srivastava et al., 2017) thanks to the high temporal (shorter than 10 s) and high spatial (smaller than 0.2 arcsec) resolution of the Solar Optical Telescope (SOT) onboard the *Hinode* satellite (Kosugi et al., 2007), and ground-based observatories, such as the Swedish 1-m Solar Telescope/CRisp Imaging SpectroPolarimeter (SST/CRISP; Scharmer et al. 2003, 2008). The reason why they were able to detect wave propagations is because the wavelengths of these oscillations are shorter than the typical spicule height. Particularly, Okamoto & De Pontieu (2011) found not only upward but also downward propagation and standing waves for the first time by using the automatic spicule axis detection method. They concluded that high-frequency waves are not sufficient for coronal heating because most high-frequency waves are reflected at the transition region and the velocity amplitudes of the waves are so small.

To solve the coronal heating problem, the transported energy to the corona needs to be evaluated quantitatively with as few assumptions as possible. The velocity amplitude is an important parameter to evaluate the transported energy flux. Spectroscopic observation is a direct way to derive the velocity amplitude. In this study, we analyzed the Lyα (121.6 nm) line profile of an off-limb spicule observed by Chromospheric Lyman-Alpha Spectro-Polarimeter (CLASP; Kano et al. 2012; Kobayashi et al. 2012; Narukage et al. 2015) and evaluated the Doppler velocity amplitude.

CLASP is a sounding rocket experiment that obtained Lyα spectro-polarimetric data with a 0.3 s temporal cadence for the polarization modulation (Kano et al., 2017; Ishikawa et al., 2017a). If we do not use the Stokes spectra of Q/I and U/I, we can utilize such an unprecedentedly high temporal cadence data to study the dynamics in the upper chromosphere and the transition region. The Lyα line is well suited to investigate how spicules affect the corona because it is sensitive to higher temperatures than other chromospheric lines (e.g., Ca II H, and Mg II h & k) because of the large optical thickness.

Alissandrakis et al. (2005) reported that Lyα spicules exhibit a height of approximately 25 arcsec (18 Mm; 1 arcsec $\approx$ 730 km on the Sun) from the limb using the Transition Region and Coronal Explorer (TRACE; Handy et al. 1999), which are taller than the spicules observed in the visible wavelengths (e.g., 4–12 Mm in the Hα line by Pasachoff et al. 2009, and 5–10 Mm in the Ca II H line by De Pontieu et al. 2007). Teriaca et al. (2006) found intensity fluctuations of 3 and 5 minutes periods in off-limb spicules with a temporal cadence of 7.5 s using the Solar Ultraviolet Measurements of Emitted Radiation (SUMER; Wilhelm et al. 1995) but they did not discuss a shorter period than 2 minutes. In this study, we focus on the wave propagation along a spicule that can be observed spectroscopically by CLASP with an unprecedentedly high temporal cadence of 0.3 s.

2.2 Observation and Analysis

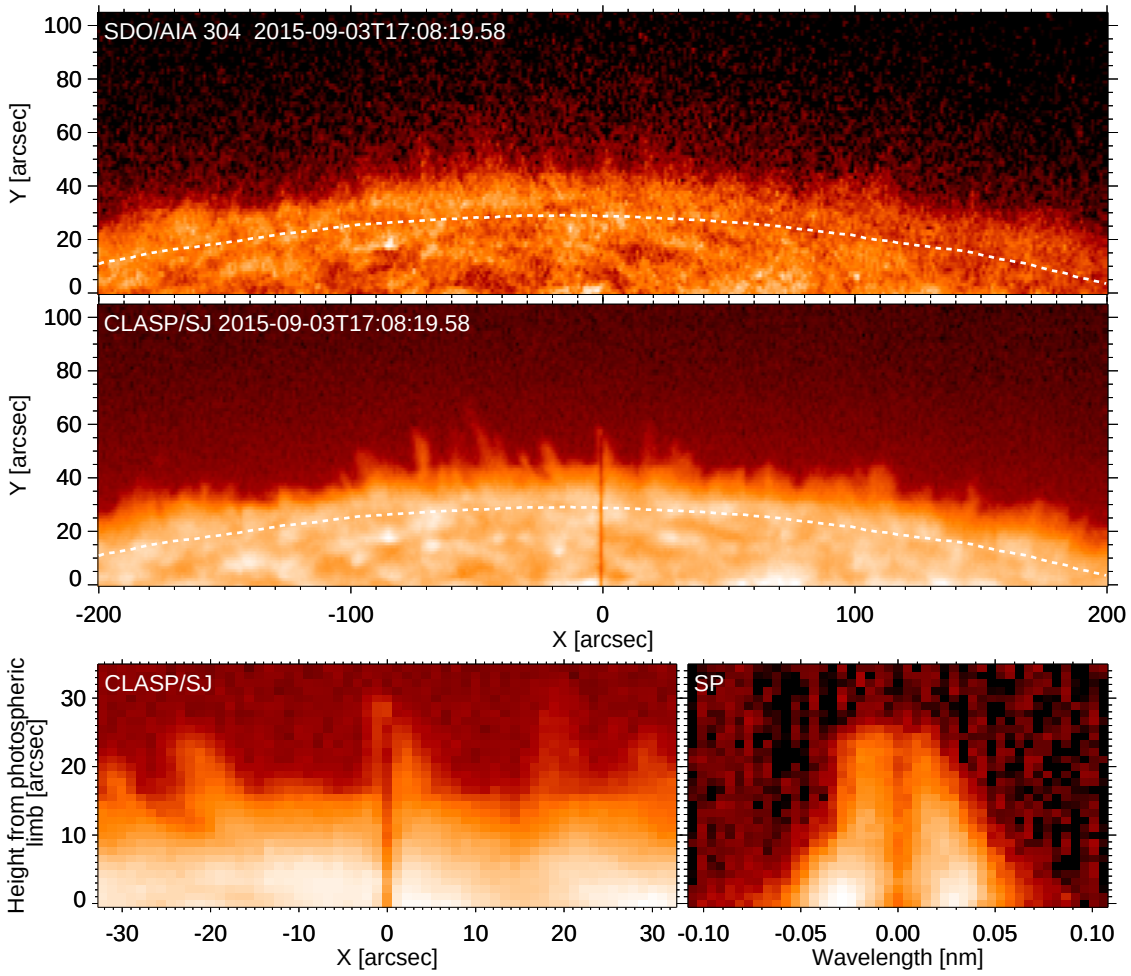

Figure 2.1: (Top) AIA 30.4 nm filter image. (Middle) Same field of view of Lyα filter image taken with CLASP/SJ as the top panel of AIA image. A vertical black line around $X = 0$ arcsec is the slit. Dotted lines in the top and middle panels show the position of the photospheric limb determined by the *SDO*/HMI continuum intensity. (Bottom left) Enlarged image of SJ filter image around the slit position. (Bottom right) Spectral data of the Lyα line at the slit position as a function of wavelength from the line center (121.6 nm). The vertical axis of the bottom two panels indicates height from the photospheric limb. The height $= 0$ and $X = 0$ in the bottom left panel corresponds solar-$X = 572$ arcsec and solar-$Y = -762$ arcsec on the heliocentric coordinate. These snapshots correspond to the time of the last CLASP observational image.

CLASP observed the quiet-Sun region near the limb for 277.2 s from 17:03 UT to 17:08 UT on 2015 September 3. The CLASP Spectro-Polarimeter (SP) acquired Lyα spectroscopic data with a 0.3 s temporal cadence, while CLASP Slit-Jaw (SJ) acquired Lyα filter images with a 0.6 s temporal cadence. The SP slit with a width of 1.45 arcsec was located 26 arcsec outside of the photospheric solar limb and perpendicular to the southwest limb inclined at -37° with respect to the solar north. During the observation, one spicule was located along the slit (Figure 2.1) and evolved beyond the edge of the slit. We focus on this spicule in this study. Because the duration of the CLASP observation may be shorter than the typical spicule lifetime (2–12 minutes; Tsiropoula et al. 2012), we check the behavior of the spicule before and after the CLASP observation by using the *Solar Dynamics Observatory*/Atmospheric Imaging Assembly (*SDO*/AIA; Pesnell et al. 2012; Lemen et al. 2012) 30.4 nm (He II line) filter image. The structural similarity between the SJ Lyα filter and AIA 30.4 nm filter images were reported by Kubo et al. (2016) and Ishikawa et al. (2017b) for the on-disk features. We used the *SDO*/Helioseismic and Magnetic Imager (HMI; Schou et al. 2012) continuum images to check the spicule height from the photospheric limb. Note that the spatial and spectral resolutions of CLASP SP are ~ 3 arcsec and ~ 0.010 nm, respectively (Giono et al., 2016a). From the temporal resolution of SP, the Nyquist frequency is about 1.6 Hz. However for the polarization observation, the rotation period of the wave plate is 4.8 s, and the image wobbled by the rotation. Considering its influence, we focused only on the oscillation longer than 4.8 s.

As shown in Figures 2.2 and 2.3, the profile of the Lyα in the spicule shows central reversal as commonly observed in the quiet-Sun regions (Tian et al., 2009). The presence of the central reversal in the off-limb spicule indicates the large opacity. The central 2–3 pixels in the self-reversal are also affected by the geo-coronal absorption, which came from the atmosphere of the Earth (Gouttebroze et al., 1978). Therefore, we applied the bisector method to derive the Doppler velocity from the wing of the Lyα line. As shown in Figure 2.3, in this method the Doppler velocity was determined from the bisector position between the red and blue sides of the emission line at a threshold. Because the continuum

intensity level is 10%–20% of the maximum intensity in the data, we chose 30% of the maximum intensity as the threshold. We also calculated the Doppler velocity with a different threshold (40% and 50%); however, the differences of Doppler velocity between the results with 30%, 40%, and 50% thresholds were less than 2 $\mathrm{km\ s^{-1}}$. The error in the Doppler velocity mainly comes from a photon noise. So, we estimated the error as the difference of the Doppler velocity from close threshold levels; 30%, 35% and 40%. We made an ensemble of thus derived errors of the Doppler velocity for the whole data set and derived the standard deviation of $\pm 0.6\ \mathrm{km\ s^{-1}}$ as the error in the Doppler velocity.

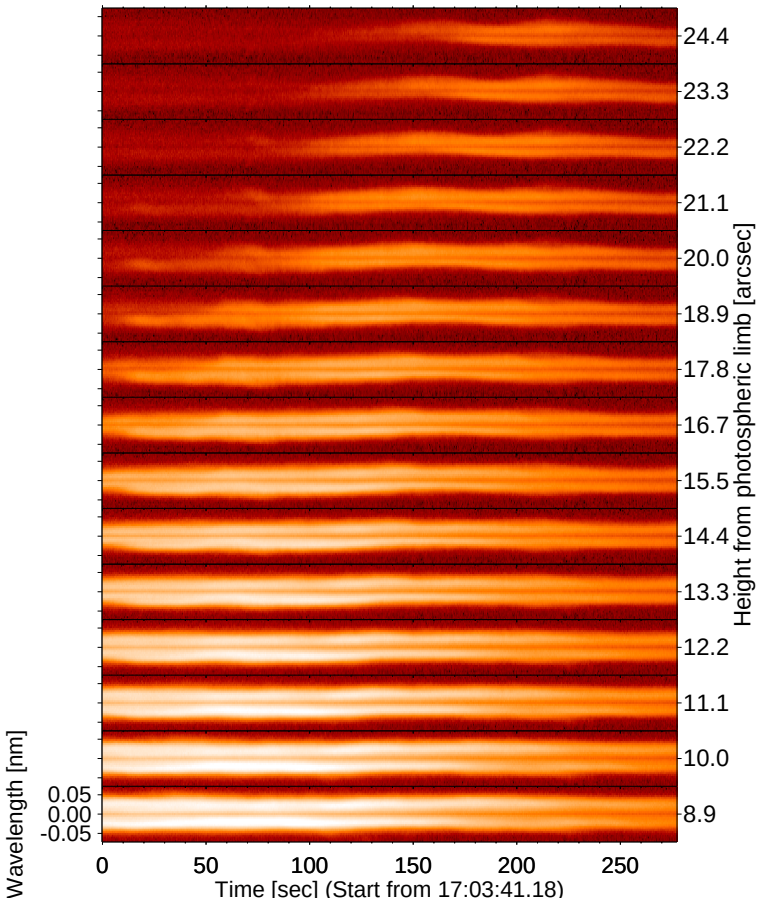

Figure 2.2: The Lyα line profile of the spicule at each height from the photospheric limb. The height step corresponds to the SP spatial plate scale (1.11 arcsec $\mathrm{pixel^{-1}}$). The horizontal axis is time, and the vertical axis in each box indicates wavelength as shown on the left side. The origin of the time corresponds to the start of the limb observation.

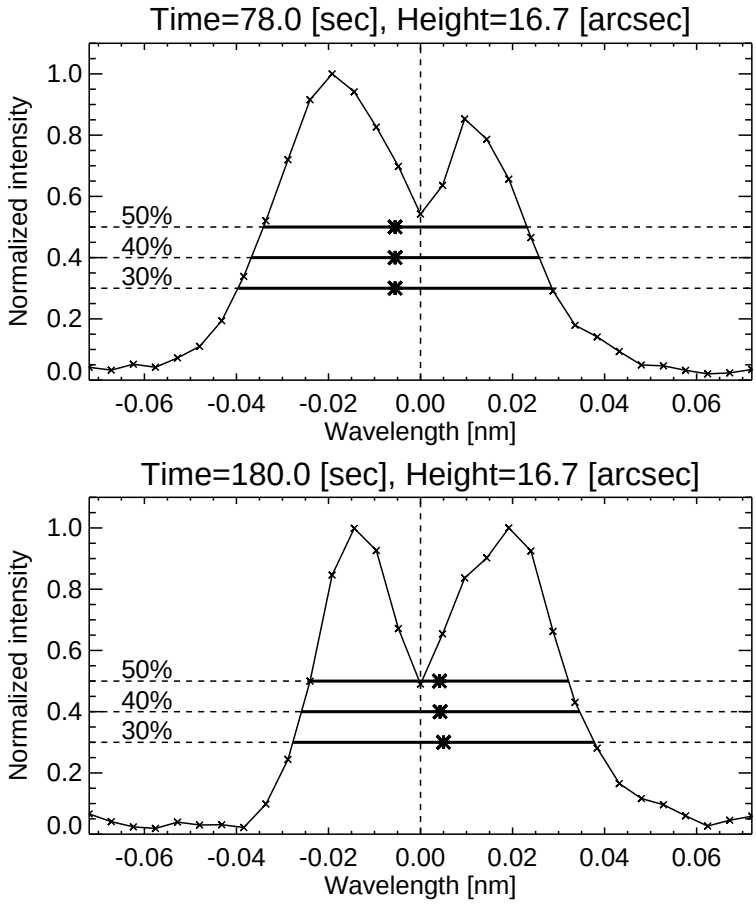

Figure 2.3: Examples of Lyα line profile at time = 78 s (Top) and 180 s (Bottom) at height $= 16.7$ arcsec height from the photospheric limb. Three asterisk symbols indicate the bisector at three different thresholds (30%, 40%, and 50%).

2.3 Results

2.3.1 Temporal Evolution of Spicule

The time-slice of the spicule in the AIA 30.4 nm filter image (left panel of Figure 2.4) shows that this spicule exhibits a lifetime of roughly 13 minutes (from 0 to 800 s time range). The white box in Figure 2.4 indicates the region and duration observed by CLASP and demonstrates that CLASP observed the clear rising motion over the time range of 0–

400 s with $30\ \mathrm{km\ s^{-1}}$. By comparing the left panel of Figure 2.4 and the right top panel of Figure 2.4 or top and middle panels of Figure 2.1, one can see that the AIA $30.4\ \mathrm{nm}$ image and the CLASP Lyα image represent the similar appearances of the spicules. However, it is also clear that the AIA $30.4\ \mathrm{nm}$ image is very noisy and hard to discuss the detail of the spicule dynamics solely with the AIA $30.4\ \mathrm{nm}$ image. As shown in the bottom left panel of Figure 2.1, the height of the spicule is about 30 arcsec, which corresponds to approximately 20 Mm from the photospheric limb. We confirmed that the spicule that we focus on is sufficiently high enough to investigate the wave propagation along it.

2.3.2 Temporal Variation of Doppler Velocity

Figure 2.2 shows the temporal variation of the Lyα spectral line at different heights of the spicule from the photospheric limb. The center of the Lyα line (central reversed part) did not shift as much. However, the wing clearly shifted in the wavelength direction.

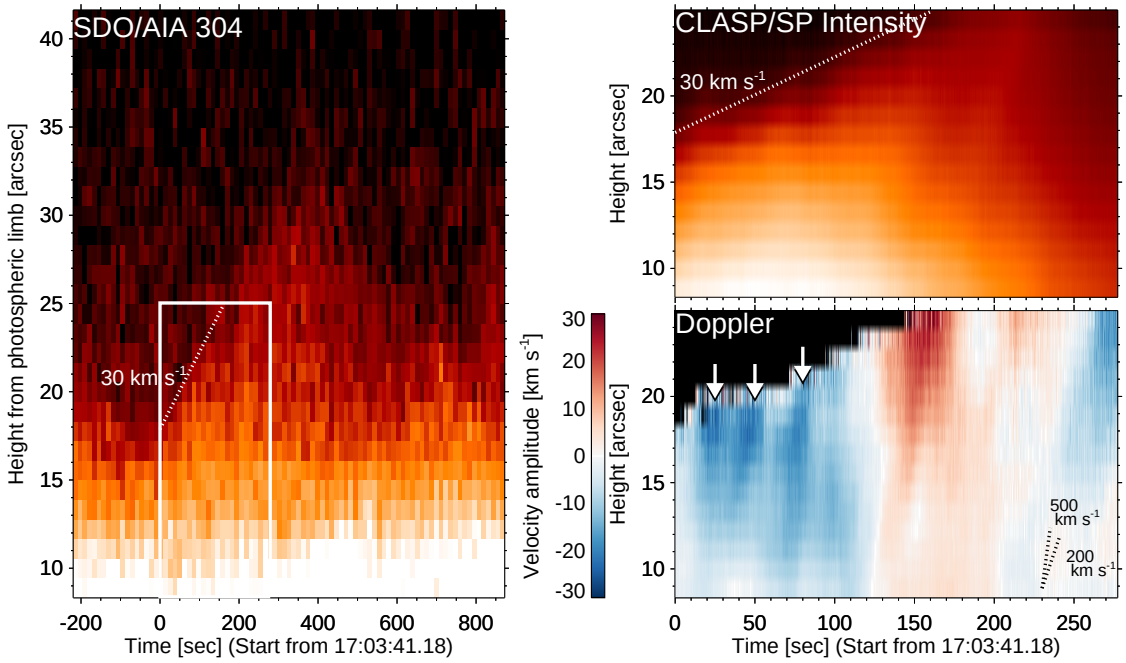

Figure 2.4: (Left) Time-slice image of the spicule observed by the AIA 30.4 nm filter. The white box indicates the height–time region corresponding to the SP spicule data (i.e., right panels.) (Top right) Height–time map of the spicule in the SP intensity. (Bottom right) Height–time map of the Doppler velocity. The top-left part of this panel colored by black is a masked area due to low intensity. The white arrows indicate the short-period velocity oscillations. In each panel, the vertical axis is the height from the photospheric limb. The white dotted lines and values in the left and top right panels indicate the spicule rising velocity. The black dotted lines and values shown in the bottom right panel correspond to the reference gradients of the phase velocity.

The lower right panel of Figure 2.4 shows the height–time map of the Doppler velocity of the spicule derived by the bisector method. The low-intensity area masked by the black color is not used in this analysis. At first, we found a long-period oscillation in this map, i.e., the blue-shift (-20 km s^{-1}) until 120 s, followed by the red-shift (20 km s^{-1}) until about 240 s, and then finally the blue shift again. The period of this oscillation is about 240 s. We also found a short-period oscillation with a period of about 30 s in the time

range of 0–100 s, as indicated by white arrows. Its velocity amplitude is about 5 $\mathrm{km\ s^{-1}}$. The ridges with large velocity amplitudes (i.e., dark blue regions) incline with time as the height increases. This indicates that these oscillations propagate in the upward direction; that is, we found the upward-propagating wave. We estimated the propagation velocity of the wave to be 200–500 $\mathrm{km\ s^{-1}}$ from the tilt of the ridges in short-period oscillations. The velocity amplitudes increase with spicule height. On the other hand, the propagation of the long-period oscillation is not clear from this observation, because the observed spicule height (~ 20 Mm) is shorter than the wavelength of the long-period oscillation of 120 Mm, where we assumed a phase velocity of 500 $\mathrm{km\ s^{-1}}$ and an oscillation period of 240 s. In the following section, we highlight the short-period oscillations.

2.3.3 Wavelet Analysis

To investigate the propagation properties of the short-period waves in detail, we applied wavelet analysis to the Doppler velocity time-series data at each height shown in the bottom right panel of Figure 2.4. Figure 2.5 shows the normalized wavelet power spectra at each height along the spicule. In this analysis, we used the wavelet analysis program by Torrence & Compo (1998). Generally, time resolution and frequency resolution are different depending on the type of mother wavelet function. In this analysis, the Morlet wavelet function, which has a good frequency resolution but poor temporal resolution, was taken as the mother function. We defined the time-dependent confidence level (so-called "global" wavelet confidence level) as a probability calculated using Monte-Carlo simulation and the background noise model as a power law plus white noise model (Auchère et al., 2016). In Figure 2.5, the wavelet power is normalized by the background noise. The area encircled by a thick black line indicates a confidence level larger than 99%. This level means that such an event is expected to occur in only one case in 100 random data sets. We also checked the results of the 90% confidence level; however, the results were not significantly different from the 99% results. In the time range of 0–100

s in Figure 2.5 a–c, the oscillations of frequency 33–50 mHz (20–30 s; hereafter called the 30 s wave) are prominent; their confidence levels exceed 99%. In Figure 2.5 i and j, the oscillations of 19–27 mHz (37–53 s; hereafter called the 50 s wave) exist with a relatively longer duration than that of the 30 s wave. The wavelet power of the 30 s wave is strong in the higher part of the spicule, while the wavelet power of the 50 s wave is strong in the lower part of the spicule. We also used the Paul mother function, which has good temporal resolution but poor frequency resolution, we got similar results—around 30 s period oscillations in the early phase on the upper part of the spicule and around 50 s period oscillations in the lower part of the spicule existing long duration. We do not see prominent powers exceeding the 99% confidence level in the period range from 4.8 s to 20 s. The results of wavelet analysis with a different thresholds of the bisector analysis are given in Appendix A.1 (Figure A.1).

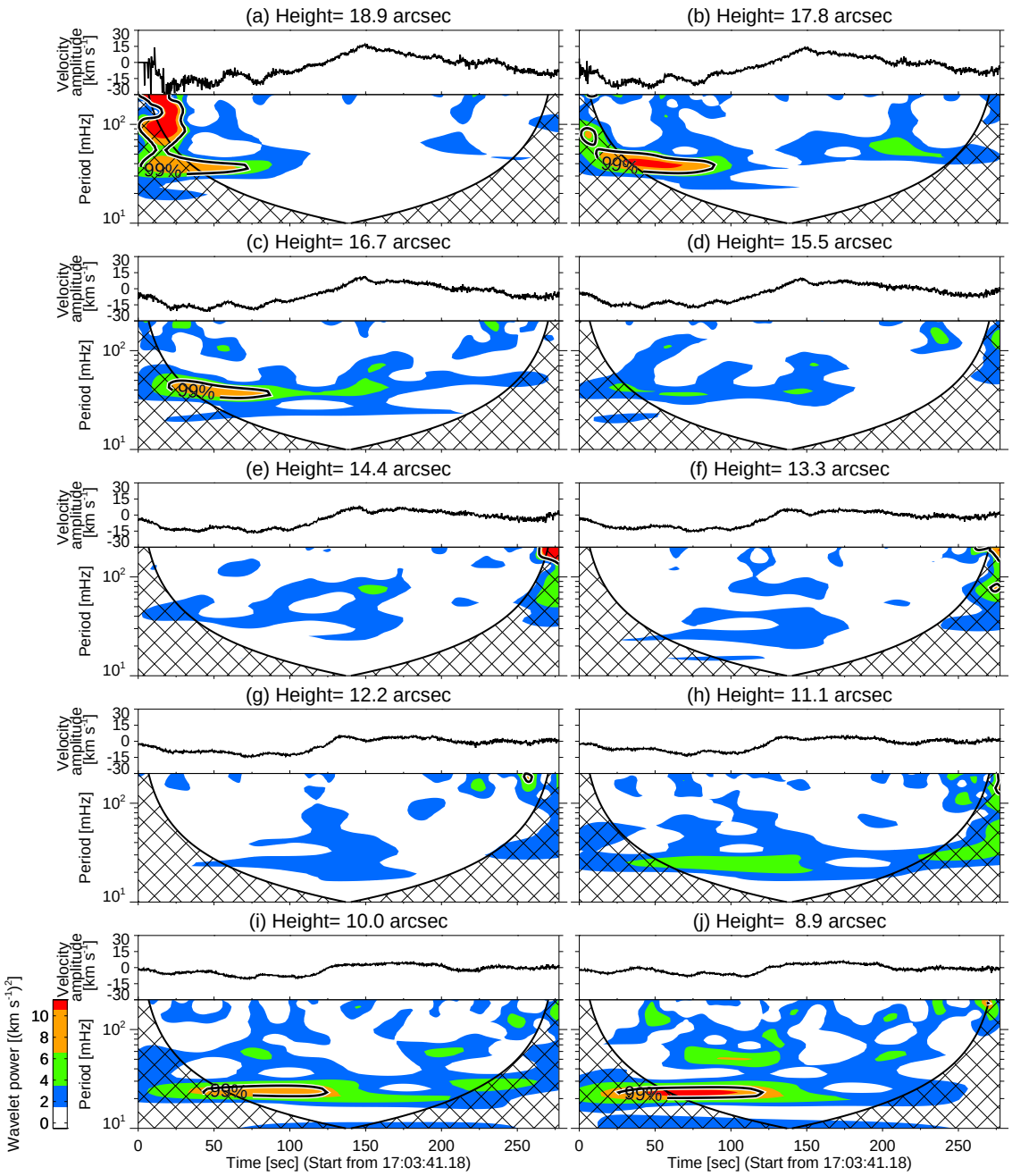

Figure 2.5: The results of wavelet analysis and curves of Doppler velocity. Each panel indicates the result at a different height from the photospheric limb. Cross-hatched areas correspond to the cone-of-influence, which is affected by the edge (discontinuity at the start timing and end timing). Areas covered by a thick black line correspond to the 99% confidence level.

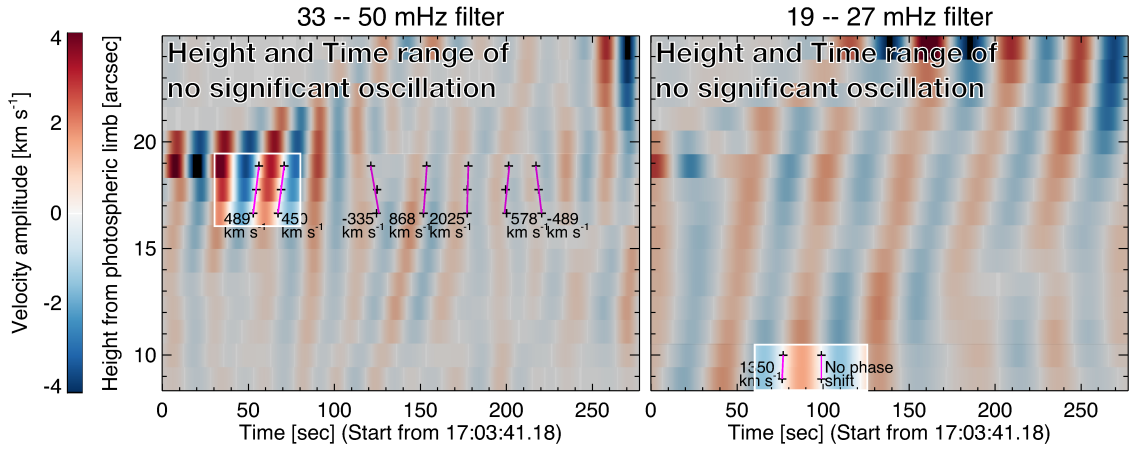

Figure 2.6: The result from the 30 s wave filter (33–50 mHz; Left) and 50 s wave filter (19–27 mHz; Right). The gray masked area corresponds to the height or timing at which there is no 99% significance wavelet power in each frequency range. The purple lines and values indicate the phase velocity calculated by linear fitting of zero-crossing timings.

To extract the wavelet power of the 30 s wave and the 50 s wave, we applied a box-type frequency filter of 33–50 mHz and 19–27 mHz frequency range, respectively, and then applied the inverse wavelet (Figure 2.6). In this figure, the regions covered with gray color correspond to the height and time ranges where there is no 99% significance wavelet power. Only a few areas are reliable in terms of velocity amplitude and phase velocity based on the wavelet analysis with confidence-level calculation.

From the results of the 30 s wave filter (left panel), the waves with a velocity amplitude of $\sim$ 3 $\mathrm{km\ s^{-1}}$ propagate upward with a phase velocity of $\sim$ 470 $\mathrm{km\ s^{-1}}$ on average in the time range of 30–80 s. In addition, the velocity amplitude of the wave gets larger with height (from ± 2 $\mathrm{km\ s^{-1}}$ at 16.7 arcsec to ± 3 $\mathrm{km\ s^{-1}}$ at 18.9 arcsec). Meanwhile, after 100 s to the end of the observation, the velocity amplitude of the 30 s wave became significantly small (less than 2 $\mathrm{km\ s^{-1}}$) and the confidence level became lower than 99%. Therefore, it is true the phase velocity is not reliable in this latter time range, but both upward and downward propagations might exist here as well as the standing waves, which do not exhibit a clear phase shift along the height direction (i.e., higher than 1000 $\mathrm{km\ s^{-1}}$).

From the results of the 50 s wave filter (right panel), standing waves with no clear phase shift were observed with the 99% confidence. The velocity amplitude of these waves is also prominent in the early phase, but small ($\sim 2\ \mathrm{km\ s^{-1}}$) compared with the 30 s waves.

2.4 Discussion

In this study, short-period (20–50 s) waves with a small velocity amplitude of 2–3 $\mathrm{km\ s^{-1}}$ were found, as well as long-period (~ 240 s) oscillation with a large velocity amplitude of $\sim 20\ \mathrm{km\ s^{-1}}$. The upward-propagating wave was also found in the short-period waves, especially around the period of 30 s, although it is not clear whether the latter long-period waves propagate along the spicule or not. Previous studies (De Pontieu et al., 2007; He et al., 2009; McIntosh et al., 2011; Okamoto & De Pontieu, 2011; Srivastava et al., 2017) have reported these oscillation components separately; however, this is the first time that both oscillation components were detected simultaneously. This is because the velocity amplitudes of a long spicule are successfully obtained directly from the spectroscopic data in the Lyα line.

In this section, we will discuss the physical properties of the long-period oscillation and the short-period waves focusing on how they are formed and how they affect the corona.

2.4.1 Long-period Oscillations

De Pontieu et al. (2007) reported oscillations with a period of 100–500 s and a velocity amplitude of 10–25 $\mathrm{km\ s^{-1}}$ in spicules, from the comparison between the observation of the lateral motion of spicules and the Monte-Carlo simulation. Tomczyk et al. (2007) and Tomczyk & McIntosh (2009) found long-period (5 minutes) propagating waves in the corona using the Coronal Multi-channel Polarimeter (CoMP) instrument. However, their velocity amplitude was measured to be less than $1\ \mathrm{km\ s^{-1}}$ and much smaller than what

was inferred from the chromospheric observations by De Pontieu et al. (2007). Tomczyk et al. (2007) speculated that the velocity amplitudes are suppressed due to the superpositions of the structures along the line-of-sight direction in CoMP observations, resulting in the large discrepancy in the velocity amplitudes between the chromosphere and the corona. In fact, nonthermal velocity derived from the CoMP line width is $30\ \mathrm{km\ s^{-1}}$ and is comparable to the velocity amplitude that was found in our observation, where the superposition along the line of sight is unlikely. Therefore, there is a possibility that the long-period oscillation in our observation is a chromospheric counterpart of the propagating waves in the corona.

The period of the long-period oscillation is on the order of the photospheric convection time-scale, approximately 3–5 minutes (Matsumoto & Kitai, 2010). One explanation is that the convective motion would oscillate the magnetic flux tube; then, the line-of-sight component of the oscillation is observed as the Doppler motion.

2.4.2 Short-period Waves

Okamoto & De Pontieu (2011) reported oscillation periods peaking near 40 s from statistical analysis using the *Hinode*/SOT filtergraphic data. They derived a median velocity amplitude of $7\ \mathrm{km\ s^{-1}}$ using the apparent transverse oscillation amplitude and period of the spicules, assuming the oscillation follows a sinusoidal pattern. Our observed period derived from Doppler motion (20–50 s) is almost consistent with their observation. Our observed velocity amplitude is slightly smaller than their reported value. One of explanations for our smaller velocity amplitude would be the difference in spatial resolution between CLASP/SP (~ 3 arcsec; Giono et al. 2016a) and the *Hinode*/SOT (~ 0.2 arcsec; Suematsu et al. 2008). The lower spatial resolution causes the smearing and underestimation of the velocity amplitudes.

The phase velocity ($\sim 470\ \mathrm{km\ s^{-1}}$) of the 30 s wave is roughly consistent with the Alfvén velocity in the upper chromosphere where we assumed a magnetic field strength

of 10 G (Trujillo Bueno et al., 2005) and a spicule density of 6×10^{-15} g cm^{-3} (at 18 Mm height from the photosphere; Beckers 1968). We derived the fast phase velocity (i.e., higher than 1000 km s^{-1}) in this study, and recognized them as a standing wave by considering the observed phase difference. Since 1000 km s^{-1} is much higher than the Alfvén velocity in the chromosphere, such recognition looks reasonable from the viewpoint of the physical property in the chromosphere.

Upward-propagating waves with a large velocity amplitude were observed, especially in the initial phase of the spicule evolution. This result implies that the source of these waves would be related to the formation of the spicule. Spicule formation by waves has been reported in a number of previous studies by numerical simulation. Kudoh & Shibata (1999) reported that the turbulent convective motions in the photosphere generate Alfvén waves, which excite longitudinal waves through the nonlinear coupling effect, lifting up the transition region to form a spicule. Shoda & Yokoyama (2018) reported that the longitudinal waves exited by the convective motion also generate short-period transverse waves and spicules by mode conversion. The period of the transverse waves generated by this mechanism is determined by the scale height of the plasma $\beta = 1$ layer where the mode conversion occurs, and is calculated to be several tens of seconds, which is consistent with our finding.

Chitta et al. (2012) reported high-frequency motion in the photosphere with a high cadence observation of 5 s by SST. They measured the motion of small-scale bright points with a correlation tracking method and derived a correlation time as 22–30 s. This timescale is consistent with our observed wave period. Similar to long-period oscillations, if the high-frequency turbulent photospheric motion would oscillate the magnetic flux tube, then the line-of-sight component of the high-frequency oscillation could be observed as the Doppler motion.

Time dependence of the wave propagation has been reported in Okamoto & De Pontieu (2011). They observed standing waves at the beginning of the spicule evolution, upward waves in the growing phase, and then standing waves again in the latter half of

the evolution. They interpreted that waves generated near the base of the spicule are immediately reflected at the transition region (top of the spicule) at the beginning. However, a time lag until the reflection appears and increases during the growth of the spicule. Finally, the reflection becomes effective in the latter half again. This interpretation is one possibility, and it is consistent with our observation of the 30 s waves if the middle phase and the latter half of the spicule evolution in their results can correspond to earlier and later than 100 s in our observation, respectively. The early phase in their results might have occurred before the CLASP observation time.

It should be noted that there is a possibility that these oscillation signatures are just transient events. In this observation, we clearly observed oscillatory phenomena of three velocity peaks shown as the three white arrows in bottom right panel of Figure 2.4. However if there are transient phenomena, we cannot ignore the possibility of random events. To solve this question, we have to observe many oscillatory phenomena and answer it statistically.

2.4.3 Energy Flux to the Upper Atmosphere

We estimated an upward energy flux of the 30 s waves in the time range of 0–100 s as approximately 3×10^4 erg cm^{-2} s^{-1} based on the result of the wavelet analysis in the left panel of Figure 2.6. We derived this value from the observed velocity amplitude as 3 km s^{-1}, the observed phase velocity as 470 km s^{-1}, and the assumed spicule density as 6×10^{-15} g cm^{-3} (18 Mm height from the photosphere; Beckers 1968). It is smaller than the required value for coronal heating in a quiet Sun (3×10^5 erg cm^{-2} s^{-1}; Withbroe & Noyes 1977). They estimated the spatially and temporally averaged energy for heating the quiet-Sun corona, while we only estimated energy transported along a single spicule, especially in the early phase of the spicule evolution. Therefore, the discrepancy between our evaluated energy flux and the required flux might become larger.

However, CLASP has a not-so-high spatial resolution (~ 3 arcsec), and a relatively

wide slit (1.45 arcsec) compared with the spicule width of ~ 0.4 arcsec (Pereira et al., 2012). Consequently, there is a possibility that multiple wave components were observed simultaneously, affecting the underestimation of the velocity amplitude. There is another possibility that not only the short-period waves but also the long-period waves with large velocity amplitude contribute coronal heating. For rigid conclusion in energy flux, detailed analysis of spectroscopic data with high spatial resolution should be conducted in the near future.

In our observation, upward-propagating waves were clearly found with the large velocity amplitude, while downward propagating waves and standing waves may exist only in the latter time period with the small velocity amplitude. Therefore, we can conclude that the contribution of the downward propagating wave is small from the viewpoint of energy transport.

2.5 Summary and Conclusions

CLASP is a sounding rocket experiment to obtain spectro-polarimetric data of the Lyα line in 5 minutes observations. During this observation, CLASP succeeded in obtaining amazing data sets of the Lyα line profiles along a spicule with 0.3 s temporal cadence. This observation enables us to detect the velocity field along a spicule. We found long-period oscillation with a period of about 240 s and short-period oscillations with a period of 20–50 s. In short-period oscillations, wave propagation is clearly found along the spicule. Thanks to the high temporal cadence observation, time-dependent properties of the short-period waves were investigated in greater detail. In the initial phase of the spicule evolution, upward-propagating waves with large velocity amplitudes were observed. These high-frequency waves might be related with the formation of the spicules, and the origin of these waves needs to be clarified.

To this end, further observations as well as the detailed comparison with the numerical simulation are required. The wave origin is not clear in our study, because in our

observation, none of shock waves or foot-point motions were observed. Such features may be hidden by high opacity in the Lyα line. We cannot derive the rigid conclusion of the wave energy. We have to estimate the transported energy, both short-period and long-period waves. To investigate the wave origin and its energy, we must observe the spicule spectroscopically, using various temperature-sensitive lines as well as the Lyα line for covering the entire spicule from the foot-point to the top and also coronal emission lines.

Hopefully, further observations with high cadence and high spatial resolution will reveal the answer. In the next Japanese solar observation satellite *Solar-C_EUVST* mission, 0.2 s of cadence and 0.4 arcsec spatial resolution is being considered for the Lyα line. It will observe not only the Lyα line with high spatial and spectral resolution, but also many emission lines from a wide temperature range simultaneously. It will be possible to investigate the propagation of waves from the lower part of spicules to the upper part in more detail.

Chapter 3

Magnetic Field of a Spicule

3.1 Introduction

Various dynamical activities triggered by magnetic fields occur in the solar atmosphere. In particular, the atmospheric layer, named the chromosphere, and the transition region are intermediate layers between the cool photosphere of temperature $6,000$ K and the hot corona of 10^6 K. Meanwhile, in this region, jet-like structures called spicules are observed everywhere. Spicules have been studied in terms of their formation mechanism (Yurchyshyn et al., 2013; Deng et al., 2015; Samanta et al., 2019) and magnetohydrodynamic wave propagation in the chromosphere (De Pontieu et al. 2007; Okamoto & De Pontieu 2011; Yoshida et al. 2019, and references therein), important factors in the heating of the corona.

To investigate the origin of the spicule and its impact on coronal heating, it is necessary to measure its magnetic field. The magnetic field measurements of a spicule have been carried out using the He I triplet lines at 1083.0 nm in the infrared. Although the field strength of the spicule is expected to be very weak, owing to the longer wavelength, the longitudinal Zeeman effect (circular polarization) can be measured, as the Zeeman splitting is proportional to the square of the wavelength. In these spectral lines, in addition to the Zeeman effect, the Hanle effect, which is generally sensitive to weak magnetic

fields and is not affected by the broadening of spectral lines, can operate. Trujillo Bueno et al. (2005), Centeno et al. (2010), and Orozco Suárez et al. (2015) carried out spectropolarimetric observations of spicules using the He I triplet lines and found a magnetic field strength of 10–80 G. In particular, Orozco Suárez et al. (2015) found that the magnetic field of spicules decre ases with height. Another spectral line used to characterize the magnetic field of a spicule is the He I D_3 line at 587.6 nm. Using this line, López Ariste & Casini (2005) compared the inclination of the magnetic field of spicules with the apparent direction of spicules identified with the imaging observation and found that the magnetic field aligns with the spicule structure. However, because the formation of the He I triplet and He I D_3 lines require excitation by ultraviolet emission from the corona (Avrett et al., 1994), it is difficult to perform an observation in a quiet region. In fact, the observation areas of López Ariste & Casini (2005) and Orozco Suárez et al. (2015) were close to the active region. In the case of quiet region observations (Centeno et al., 2010), they temporally integrated data over a time span of 45 minutes to earn a sufficient signal-to-noise ratio. However, recent spectroscopic observations revealed very rapid spicule phenomena on the time scale of several tens of seconds of the spicules that is considered to the evolution of the magnetic field (Okamoto & De Pontieu, 2011; Yoshida et al., 2019). Hence, spectropolarimetric observation using bright spectral lines is necessary for investigating the temporal evolution of the magnetic field, even in the quiet region.

The temperature from the upper chromosphere to the transition region is 10^4–10^5 K, and there are abundant spectral lines that originate from these atmospheric layers in the ultraviolet wavelength region. Štěpán & Trujillo Bueno (2011), Trujillo Bueno et al. (2011), and Belluzzi et al. (2012) reported that the core of the Lyα line (wavelength range of 121.57 ± 0.014 nm), which is the brightest spectral line in the vacuum ultraviolet range and observable everywhere on the Sun, is sensitive to the Hanle effect with a field strength of 10–250 G. This sensitivity range is comparable to the field strengths of spicules reported in previous studies. Therefore, spectropolarimetric observations of the Lyα line would enable the measurement of the magnetic field of spicules using the Hanle

effect. Because the wavelength of the Lyα line is short and the spectral line is broad, the polarization signals induced by the Zeeman effect cannot be measured.

The Lyα line is absorbed in the Earth's atmosphere; thus, observation from space is necessary. We use data from the Chromospheric Lyman-Alpha Spectro-Polarimeter (CLASP) sounding rocket experiment conducted in September 2015, which has provided the first spectropolarimetric observations of the Lyα line. As discussed in Yoshida et al. (2019), CLASP successfully observed the initial phase of the evolution of an off-limb spicule. In this study, we present the first polarization spectra of an off-limb spicule in the Lyα line, obtained by CLASP. To achieve our final goal of constraining the magnetic field of the spicule, we examine the height and temporal variation of the polarization in the spicule. Then, we model the radiation field semi-quantitatively, using observational data to evaluate the scattering polarization. Finally, by comparing the estimated scattering polarization with the observation, we constrain the magnetic field of the spicule.

3.2 Observation and Analysis

CLASP observed an off-limb spicule for 277.2 s. A slit of width of 1.45 arcsec and length 400 arcsec was placed 26 arcsec off the visible solar limb. The Spectro-Polarimeter (SP) cameras took data every 0.3 s, synchronized with the polarization modulation unit, to measure the modulation. To demodulate the Stokes Q and U parameters, using the same equations shown in the Appendix of Ishikawa et al. (2017a), at least four exposures were needed; finally, the polarization data of the Lyα line were obtained with a cadence of 1.2 s.

The slit position was monitored through a Slit-Jaw (SJ) imaging system at a cadence of 0.6 s, providing observations of the Lyα line. Details of this observation are shown in our previous paper (Yoshida et al., 2019). To suppress the spurious polarization due to the fluctuation in intensity and increase the signal-to-noise ratio, we combine the two channels to derive I, Q and U. The error of the polarization signal is evaluated using

photon noise and CCD readout noise (Ishikawa et al., 2014).

In the off-limb region, the intensities of the Lyα wing (around $121.57\ \mathrm{nm} \pm 0.05\ \mathrm{nm}$) and the Si III ($120.65\ \mathrm{nm}$) lines were dark. As a result of the noise evaluation, a sufficient polarization signal could not be obtained; thus, we focus only on the Lyα core in this analysis.

3.3 Results

3.3.1 Temporally Averaged Polarization Signal

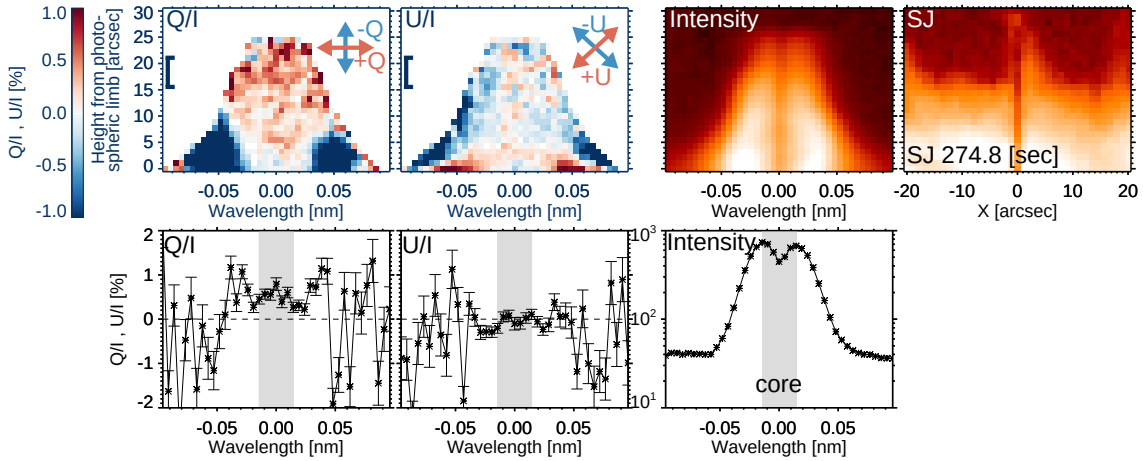

Figure 3.1: (Top) From left to right, temporally averaged Q/I, U/I, and intensity as a function of wavelength from the line center ($121.57\ \mathrm{nm}$) of the Lyα line and SJ filter image at 274.8 s after the start of the CLASP observation of the off-limb spicule. The polarization directions are defined as the arrows shown in each panel. The small signal areas are masked in the Q/I and U/I map. Height $= 0$ corresponds to the height of the photospheric limb observed by the *Solar Dynamics Observatory*/Helioseismic and Magnetic Imager (*SDO*/HMI; Pesnell et al. 2012; Schou et al. 2012) continuum image. (Bottom) Spatially averaged (height range of black bracket) profiles of the Q/I, U/I, and intensity. The Lyα core ($121.57\ \mathrm{nm} \pm 0.014\ \mathrm{nm}$) is marked in gray color.

Figure 3.1 shows the temporally averaged polarization spectra over 277.2 s above the limb, observed by visible light. The SJ image (right top panel of Figure 3.1) shows that the off-limb spicule reached as height as 30 arcsec above the limb, with the slit edge located at 27 arcsec. The polarization directions parallel and perpendicular to the nearest solar limb are defined as positive and negative Q, respectively. The positive and negative Stokes U are defined as rotated 45° counterclockwise from the Stokes Q. In the Lyα core, the Q/I in the off-limb spicule is dominated by a positive signal, and the amplitude is about $0.5\% \pm 0.1\%$, while U/I is dominated by a negative signal, and the amplitude is smaller than that of Q/I at $0.0\% \pm 0.1\%$ (bottom left and right panel of Figure 3.1). The linear polarization in the off-limb spicule is essentially parallel to the solar limb, which is consistent with the scattering polarization due to the radiation field from below.

In the Lyα wing, Q/I is negative at a height of about 10 arcsec from the photospheric limb. Kano et al. (2017) reported the center-to-limb variation (CLV) in which the Q/I is negative for the Lyα wing on the solar disk, and the polarization degree increases from the disk center toward the limb. Because the solar limb of the Lyα line is located outside the photospheric limb, Q/I of the Lyα wing is negative at the low height of the spicule, owing to the CLV.

3.3.2 Temporal Variation of Polarization Signal

In this section, we focus on the temporal variation of the polarization signal as a function of height. To increase the signal-to-noise ratio, we integrated over the wavelength range in the Lyα core (121.57 ± 0.014 nm), over which the emissions are from the same height and have the same mean free path (Ishikawa et al., 2017a). In the time direction, we used Q/I and U/I data sets running-averaged over 28.8 s, which corresponds to the 6-rotation period of the rotating wave-plate. The three right panels of Figure 3.2 show the height–time variation of the intensity, Q/I, and U/I of the Lyα core. From the panels of the Q/I and U/I plots, the polarization degree of Q/I and U/I are shown to be larger in the

height range from the height of the surrounding spicule (height $= 15$ arcsec) to top of the spicule (hereafter, referred to as the upper-part) than in the height range from height $= 0$ to the height of the surrounding spicule (hereafter, referred to as the lower-part). In the upper-part, we found the Q/I signal to be positive (about $+0.5\%$); meanwhile, the U/I signal changes from positive (about $+0.5\%$) to negative (about -0.5%). To focus on the height variation, we integrated in the height direction, dividing the range into the lower- and upper-part of the spicule.

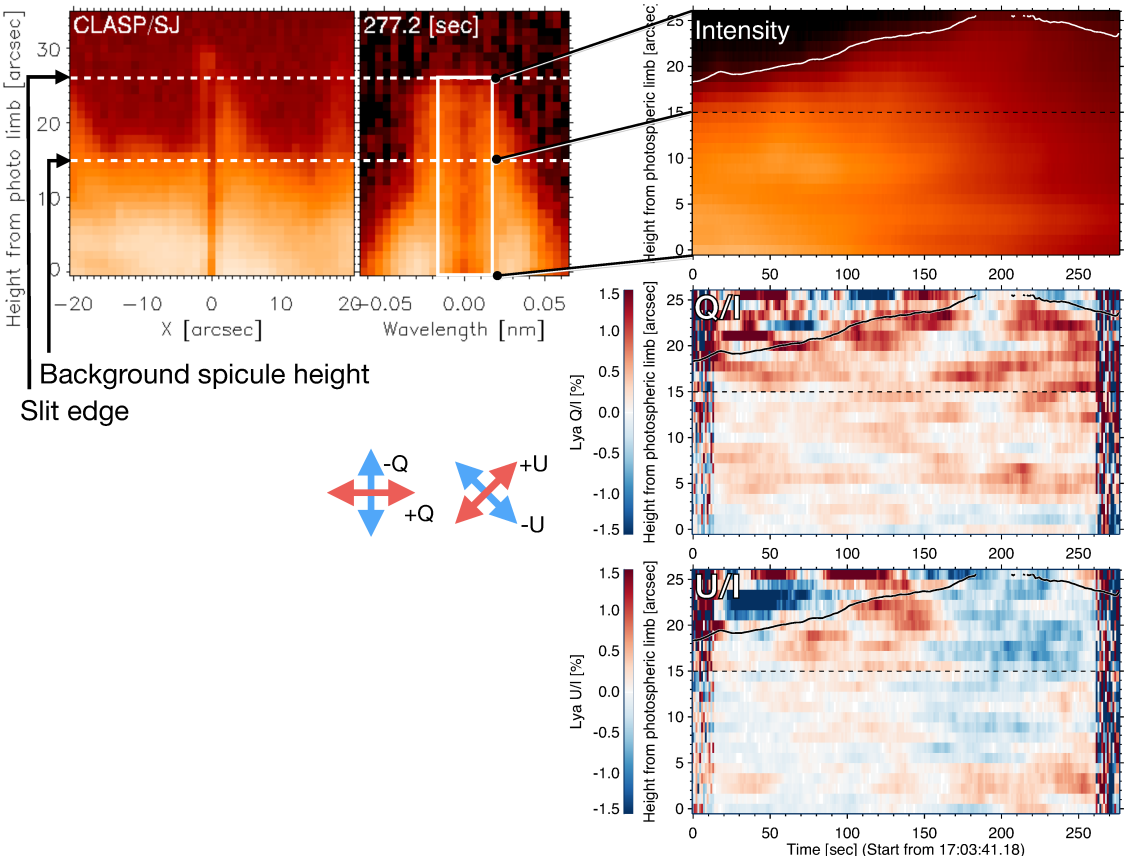

Figure 3.2: (Left) The snapshot of the SJ and SP observation data. The upper and lower white dotted lines are the height of slit edge and background spicules, respectively. (Right) Height–time variation of the Lyα intensity, Q/I, and U/I from top to bottom in the range of white box shown in SP image. The initial and final 28.8 s time ranges in the Q/I and U/I panels are affected by edge effect due to the running average. The white line shown in intensity plot, which is as same as black line shown in Q/I and U/I plot, corresponds to the trace of the motion of spicule top. In the left 2 panels (SJ and SP images), the position of upper white dotted line, and the lower white dotted line are the slit edge, and the height at which the multiple spicules are overlapping, respectively.

Figure 3.3 shows the temporal variation of the Q/I and U/I signals in the Lyα line with a 28.8 s (6-rotations of wave-plate) running average. The red lines indicate polarization signals in the upper-part of the spicule. The dark blue lines indicate the lower-part

of the polarization signals. The Q/I and U/I signals in the upper-part are stronger than those in the lower-part. In the upper-part, Q/I is about $+0.5\%$, and U/I changes from $+0.5\%$ to -0.5%. Meanwhile, in the lower-part, both Q/I and U/I signals are close to 0% ($Q/I \sim 0.2\% \pm 0.1\%$ and $U/I \sim 0.0\% \pm 0.1\%$). The accuracy of the polarization signal is 0.1%–0.3%, mainly because of the photon noise.

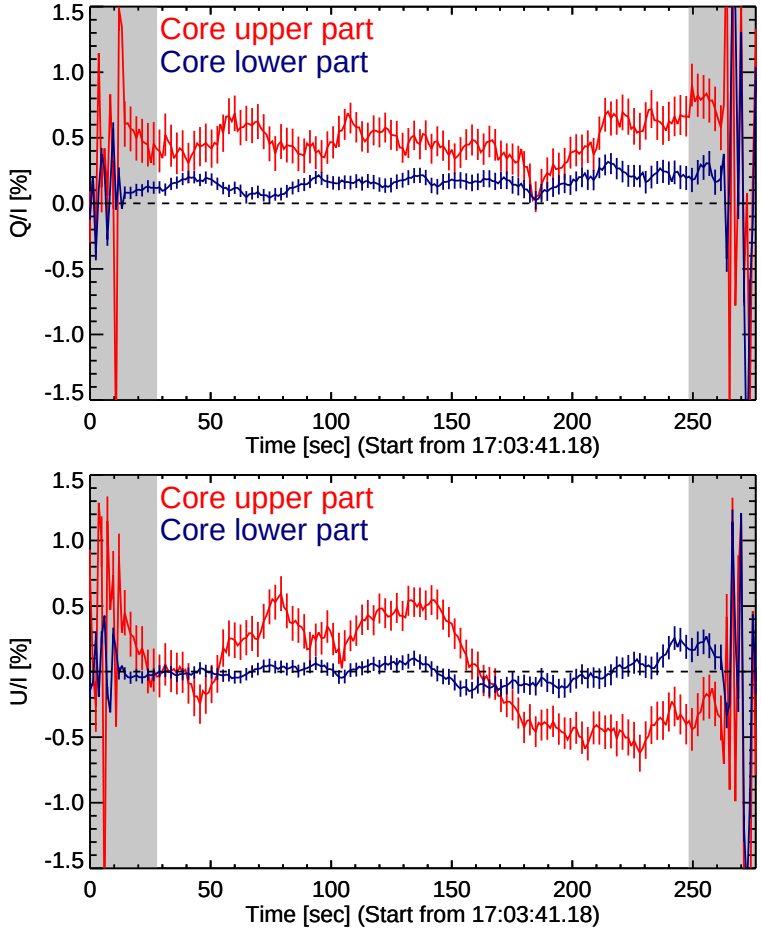

Figure 3.3: Temporal variation of Q/I (top) and U/I (bottom) with a 28.8 s running average. The red and dark blue lines correspond to the spicule upper and lower-parts, respectively. Each error bar is calculated based on the photon noise and CCD read-out noise. The initial and final 28.8 s time ranges are masked with gray color, since it affected by the edge effect due to the running average.

Figure 3.4 shows the temporal variation in the direction of linear polarization (indi-

cated by the angle θ_p from the X-axis direction of the SJ image in Figure 3.2) obtained using the following equation.

$$\theta_p = \frac{\tan^{-1}\left(\frac{U/I}{Q/I}\right)}{2}. \tag{3.1}$$

As shown in the change in U/I, the polarization direction changes from about $+20^\circ$ to -20° over time. Here, the error bar is obtained from the respective errors of the Q/I and U/I signals and is about 7°.

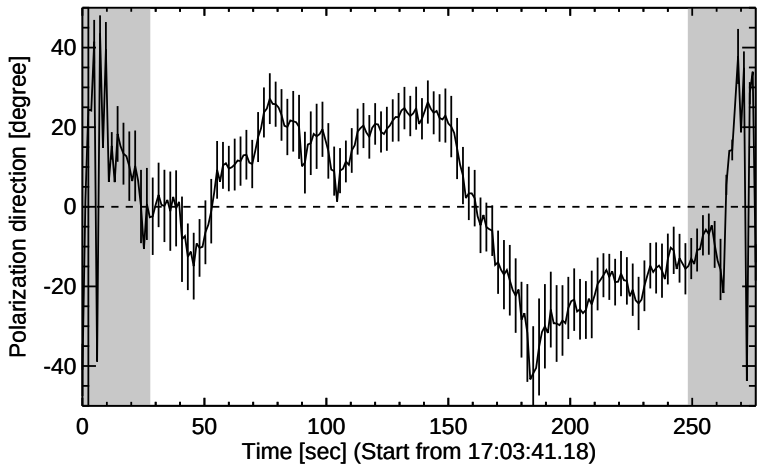

Figure 3.4: Temporal variation of the polarization direction with respect to the X-axis of the SJ image in the Figure 3.2 calculated by Equation (3.1). The error bar is calculated based on the error of the Q/I and U/I signals.

Next, to compare the polarization direction and inclination of the spicule, we examined the temporal variation in the spicule structure seen in the SJ image. From Figure 3.5(a–f), the spicule has an inclination of 10–30° with respect to the X-axis. Even when the temporal variation is considered, the temporal variation of the spicule inclination is smaller than the temporal variation of the polarization direction. Figure 3.5(g) shows the temporal variation of the position of the spicule (integrated over the height of the upper-part) with respect to the slit position. The vertical black line indicates the slit position.

From the point of view of the observer, the spicule sways left to right with respect to the slit position. It can be seen that the position of the slit is on the right side of the spicule around 60–110 s, near the middle around 160 s, and on the left side around 200–250 s. We will discuss the relationship between the polarization direction and the spicule structure in Section 3.4.3.

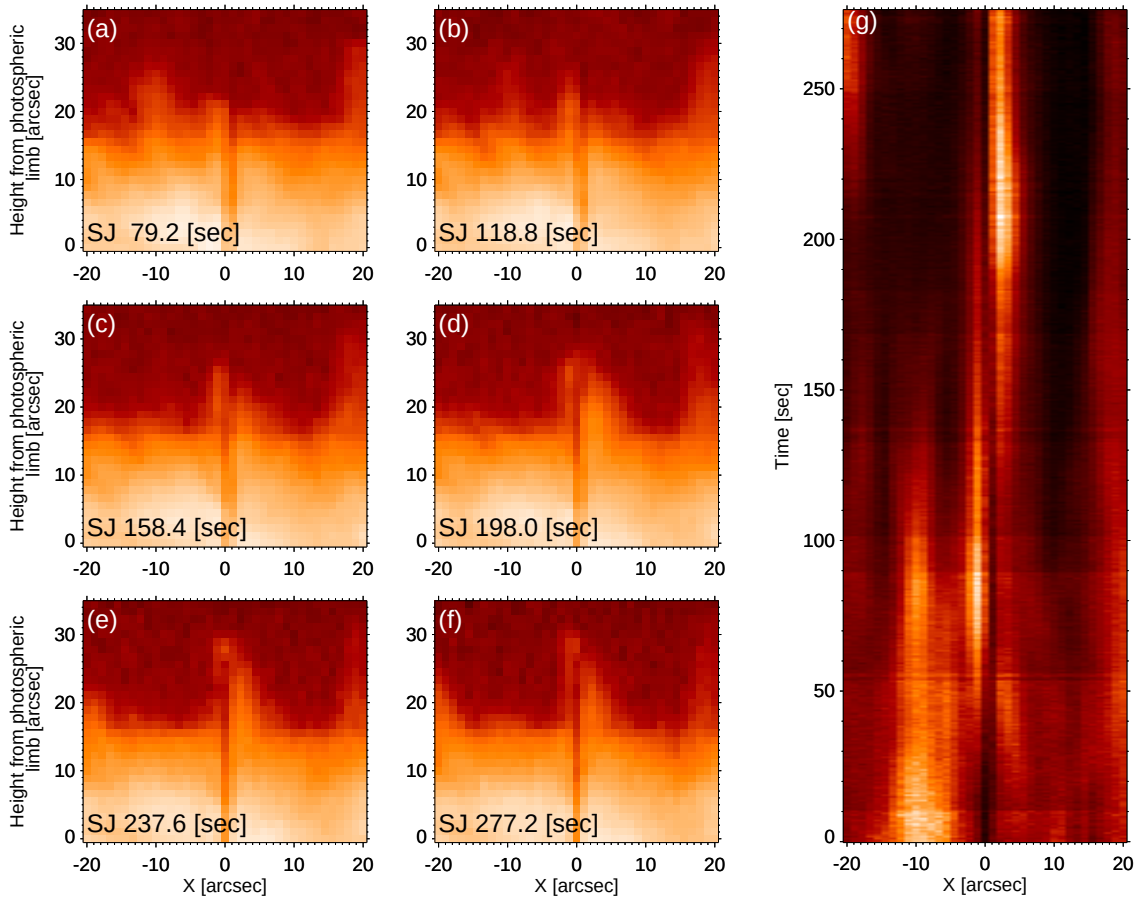

Figure 3.5: (Panel a–f) Temporal variation of the SJ images. The black vertical line at $x = 0$ is the slit position. (Panel g) Space–time plot of the SJ images. The horizontal axis of this panel corresponds that of panel a–f averaged in the upper-part, the vertical axis is time of the SJ observation period.

3.4 Discussion

The positive Q/I during the observation period indicates that the 90° scattering by the anisotropic incident radiation from the solar disk is dominant. The temporal variation observed in the U/I signal can be considered to be due to the temporal variation of magnetic field vector (i.e., operation of the Hanle effect) and/or the non-axisymmetric properties of the radiation field. We discuss possible constraints on the magnetic field in the spicules.

3.4.1 Height Variation

Considering the height variation, the polarization signals of Q/I and U/I in the lower-part are smaller than in the upper-part, as shown in Figure 3.3. This can be understood as the height variation of the spicule density. In the lower-part, because the structure is dense, the plasma of the spicule is illuminated not only in the vertical but also in the horizontal direction. Radiation from below produces a $+Q$ signal, whereas radiation from side produces a $-Q$ signal. Thus, the net polarization is small. In the upper-part, owing to the low density of the structures, the plasma of the spicule is mainly illuminated from the vertical direction (Figure 3.6). Therefore, the height variation in the polarization signal is caused by the variation in the radiation anisotropy. Consequently, the upper-part of the spicule is considered to be relatively simple, described by a plasma illuminated from below. With the motivation to investigate the influence on the corona, we discuss the magnetic field parameters, particularly in the upper-part of the spicule.

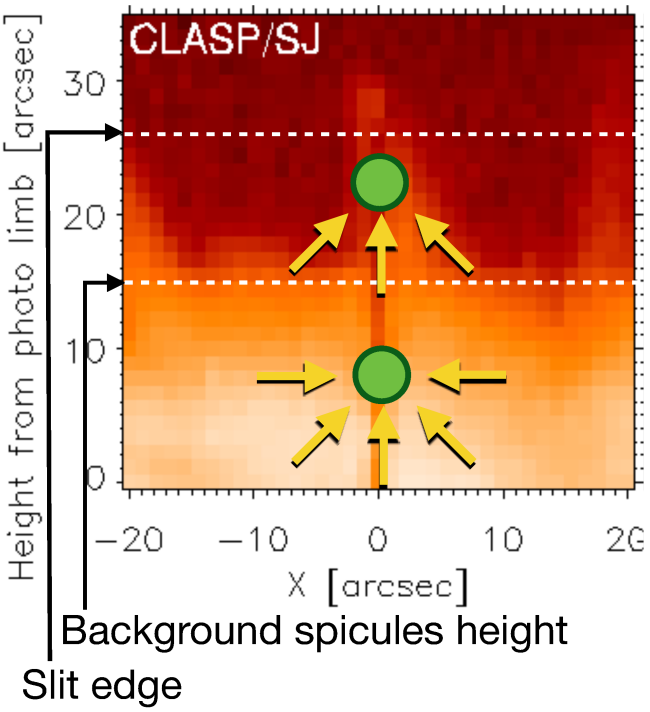

Figure 3.6: The schematic view of the difference of the illumination directions between spicule's upper-part and lower-part.

3.4.2 Magnetic Field Constraint (Axisymmetric Radiation Field)

We first discuss the magnetic field strength that can be considered from the observed values of the polarization degree when assuming an axisymmetric radiation field; then, we discuss the effect of the non-axisymmetric radiation field. To consider the effect of the radiation field, we construct a cone model as shown in Figure 3.7, assuming that the plasma in the spicule is illuminated from a certain area on the solar surface. We set the height of the cone as $h = 5$ arcsec from the surrounding spicule, assuming that the radiation of the Lyα line is emitted from the top of the surrounding spicule. Assuming that the Sun is a sphere, the extent to which radiation reaches a point outside that area is determined by the point of contact between the point and the sphere. The radius of the bottom of the cone is determined from its point of contact as $r_{max} = 100$ arcsec.

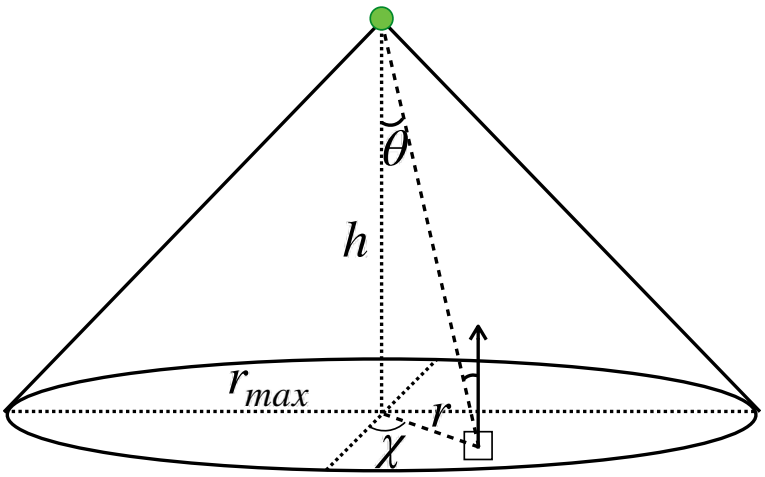

Figure 3.7: Cone model of the radiation field. The spicule's plasma located top (green circle) illuminated from the base of the cone. The cone height h and radius of the cone base r_{max} are defined from the geometry of the SJ image.

The parameters of the axisymmetric radiation field are represented using radiation field tensors, given by the following equations for J_0^0 and J_0^2 (Eq. (5.157) of Landi Degl'Innocenti & Landolfi 2004).

$$J_0^0 = \oint \frac{d\Omega}{4\pi} I(\vec{\Omega}) \tag{3.2}$$

$$J_0^2 = \frac{1}{2\sqrt{2}} \oint \frac{d\Omega}{4\pi} (3\cos^2\theta - 1)\, I(\vec{\Omega}), \tag{3.3}$$

where $I(\vec{\Omega})$ is an intensity, and $\vec{\Omega}$ is a solid angle of spicule plasma from base. In these equations, we assume unpolarized incident radiations. J_0^0 is the total radiation amount, whereas J_0^2 is the vertical and horizontal radiation imbalance with respect to Figure 3.7. We use the average value of the disk-center intensity from the SJ observation as $I(\vec{\Omega})$ in Equations (3.2)–(3.3), assuming that it is constant regardless of the solid angle. We calculated the radiation field parameter J_0^2/J_0^0 as 0.020 in which the anisotropy of the

radiation field was normalized by J^0_0. In practice, h is higher than 5 arcsec, as the radiation is likely to be emitted from a slightly lower height than the surrounding spicules. In that case, J^2_0/J^0_0 also increases. Therefore, J^2_0/J^0_0 is larger than 0.02 under this assumption.

The calculation code provided by Goto et al. (2019) is used to calculate the Q/I and U/I signals in the assumed radiation field without considering the radiative transfer equation. In this calculation, we used the last scattering approximation that evaluates polarization, considering multiple scattering by radiation from the disk as single scattering assuming an axisymmetric radiation field. The magnetic field parameters include the magnetic field strength B, inclination θ_B, and azimuth χ_B, shown in Figure 3.8. The angle θ_B represents the angle from the Z-axis, and χ_B is the angle from the X-axis on the X-Y plane.

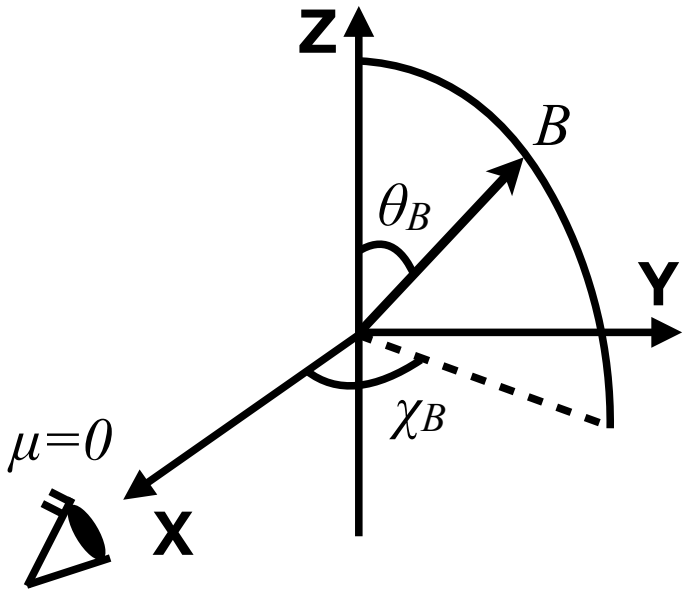

Figure 3.8: Coordinate of the magnetic field parameters. The Z-axis is normal direction of the solar surface. The X-axis is line-of-sight direction. The magnetic field vector is characterized by its strength B, inclination angle θ_B, and azimuth χ_B. The Y-Z plane corresponds the plane-of-sky. The heliocentric angle Θ ($\cos\Theta = \mu$) is fixed as $90°$, since it is off-limb observation.

We calculated the Q/I and U/I signals using a calculation code based on the value of J^2_0/J^0_0 obtained from the assumed cone model. We restricted the inclination and azimuth of the magnetic field based on the spicule inclination seen in the SJ image, assuming that the spicule is aligned along a magnetic field line. Because the temporal variation of the spicule inclination was small, we assumed that it was constant with time. Because the spicule inclination seen in the SJ image is the plane-of-sky projection (Y-Z plane in Figure 3.8), we converted the projected inclination θ'_B into the inclination of the magnetic field θ_B using the following relationship.

$$\tan\theta_B = \frac{\tan\theta'_B}{\sin\chi_B}. \tag{3.4}$$

In addition, the SJ image shows that the magnetic field is inclined in the ($-$Y, $+$Z) direction or ($+$Y, $-$Z) direction in Figure 3.8. When $0^\circ < \theta_B < 90^\circ$, the range can be limited to $180^\circ < \chi_B < 360^\circ$, and when $90^\circ < \theta_B < 180^\circ$, the range can be limited to $0^\circ < \chi_B < 180^\circ$. We cannot identify the difference in the calculation results between the direction of ($-$Y, $+$Z) and ($+$Y, $-$Z), owing to the 180° uncertainty (i.e., Q/I and U/I do not change when the magnetic field vector is rotated 180° around the line-of-sight). In the following discussion, we only calculate the direction of ($-$Y, $+$Z).

The calculation results are shown in Figure 3.9 as a Hanle diagram, in which the horizontal axis is U/I and the vertical axis is Q/I. In this calculation, we fixed $J^2_0/J^0_0 = 0.020$ in each panel. We changed the parameters of θ'_B, and the magnetic field strength B, assuming that their temporal variations are small.

As shown in Figure 3.9, both the Q/I and U/I signals decrease as the magnetic field strength increases. Similar to the magnetic field, increasing the anisotropy of the radiation field J^2_0/J^0_0 increases both the Q/I and U/I signals, whereas decreasing the anisotropy of the radiation field decreases both the Q/I and U/I signals. Assuming that the oscillation of the spicule is the Alfvén wave, the temporal variation in the polarization signal is limited in this plot, because the oscillation can be represented by a change in the

inclination and azimuth.

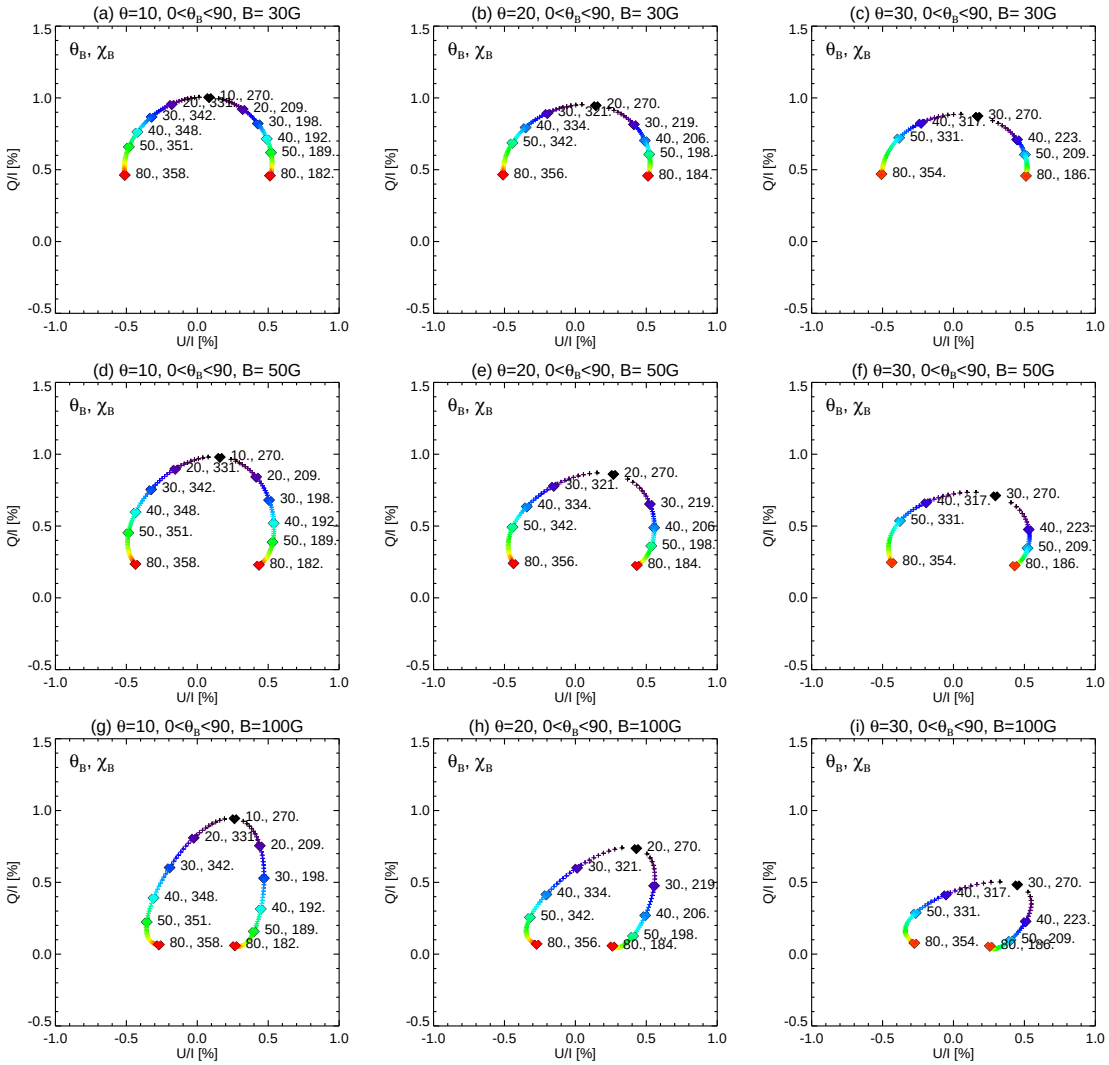

Figure 3.9: Calculated result of the Hanle diagram with $J^2_0/J^0_0 = 0.020$. The projected inclination θ'_B changes from $10°$, $20°$, and $30°$ from the left, middle, and right columns, respectively. The magnetic field strength is fixed as 30 G in the top three panels, 50 G in the middle three panels, and 100 G in the bottom three panels. The values next to the symbols in each panel are the values of θ_B and χ_B in degrees.

Figure 3.10 shows the temporal variation of the observed polarization signals in the upper-part of the spicule in the Hanle diagram. Colors represent the temporal variation from the start to the end of observation. We try to determine the magnetic field parameters

to be consistent with this Hanle diagram: the Q/I signal is almost constant about $+0.5\%$, and the U/I signal changes from $+0.5\%$ to -0.5%.

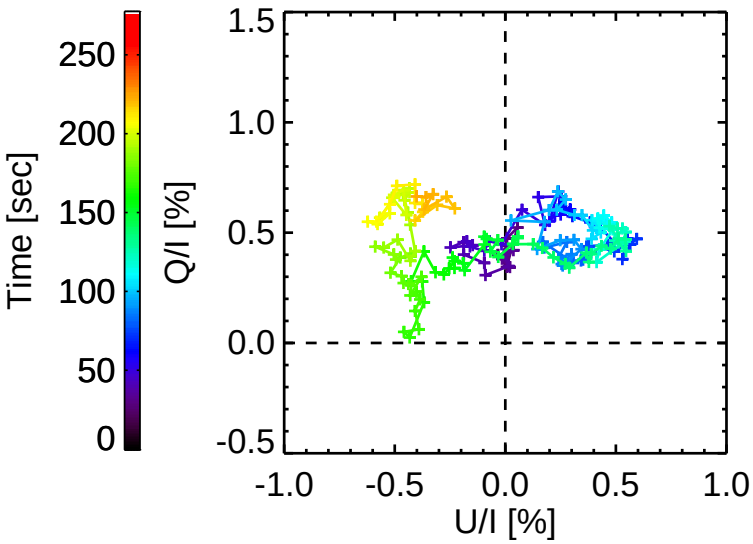

Figure 3.10: Observed polarization signals plotted on the Hanle diagram. The color represents time evolution from the start (black) to the end (red).

For example, by comparing Figure 3.9 and 3.10, when the magnetic field is 50 G and $\theta'_B = 30°$ (Figure 3.9(f)), the temporal variation of the U/I signal from $+0.5\%$ to -0.5% can be explained by the variation from $\theta_B = 40°$ and $\chi_B = 223°$ to $\theta_B = 50°$ and $\chi_B = 331°$. This angle variation corresponds to a $\sim 70°$ [1] change in the magnetic field direction. However, this is inconsistent with the result of the spicule oscillation obtained by the spectroscopic observation. Based on the low-frequency oscillation (velocity amplitude: 20 km s^{-1}, period: 240 s; Yoshida et al. 2019) found from the spectroscopic observations and a spicule height of 18 Mm, the possible change in the angle of the spicule (i.e., magnetic field direction) is $6°$ even if it is largely estimated. In addition, the value of the magnetic field strength of 50 G in the spicule upper-part is larger than expected from previous studies. Orozco Suárez et al. (2015) reported that near the active region, the

[1]The angle variation from θ_1 and χ_1 to θ_2 and χ_2 is expressed by $\cos^{-1}\left[\sin\theta_1 \sin\theta_2 + \cos\theta_1 \cos\theta_2 \cos\left(|\chi_1 - \chi_2|\right)\right]$.

magnetic field strength of the lower-part of the spicule is about 80 G but decreases with height, and the upper-part of the spicule is about 30 G. The magnetic field strength around the quiet region might be smaller than that of near the active region.

Therefore, further revision of the radiation field model is required. Considering the time-averaged observation results (Figure 3.1; $Q/I = 0.5\%$ and $U/I = 0.0\%$), it is clear that a magnetic field strength of 50 G or more is required to explain the observation results (Figure 3.9(f)). In the modeling of the radiation field around the spicule, we considered only the thermal radiation from the solar surface, assuming that the thermal radiation of the spicule was sufficiently smaller than the thermal radiation from the solar surface for simplicity. The thermal radiation from the off-limb spicule is unpolarized from the observer because radiation in the vertical and horizontal directions are balanced; $J^2_0 = 0$. However, the solid angle of the total radiation amount J^0_0 can be regarded as approximately 2π because the scatterer is located on the spicule. Assuming that the radiation from the solar surface is contributed by on-disk spicules, the thermal radiation from the spicule and the solar surface are comparable. In that case, the denominator of J^2_0/J^0_0 in the scatterer becomes 2π larger on the spicule due to the thermal radiation of the spicule. Because Q/I is approximately proportional to J^2_0/J^0_0 (Trujillo Bueno et al., 2011), it is expected that re-evaluation of J^2_0/J^0_0 in consideration of thermal radiation of spicules will yield consistent results between observations and calculation results.

3.4.3 Magnetic Field Constraint (Non-Axisymmetric Radiation Field)

We consider the effect of non-axisymmetric radiation field qualitatively. From the SJ observation (Figure 3.5), the spicule oscillated left to right with respect to the slit position with an almost constant inclination to the plane-of-sky. Figure 3.5(g) shows the slit located on the right side of the spicule in the 50–100 s time range and the slit located on the left side of the spicule in the 200–250 s time range. The period of this change coincides

with the temporal variation of U/I in the upper-part of the spicule (Figure 3.3 bottom) and the polarization direction (Figure 3.4) (i.e., about $+20^\circ$ in the 50–100 s time range and about -20° in the 200–250 s time range, with respect to the X-axis).

Assuming that the off-limb spicule in the Lyα line is sufficiently optically thick, when the slit is located on the right side of the spicule, radiation from the disk does not propagate from the left side; thus, only radiation from the spicule needs to be considered. From the intensity ratio of the brightness in the SJ image, the radiation of the spicule itself is sufficiently smaller than the radiation from the disk. Therefore, in this case, the radiation from the left side becomes weak, and the radiation from the right side becomes strong. The direction of the scattering polarization is orthogonal to the symmetrical axis of incoming radiation field. In this case, the incoming radiation field comes mainly from the right side, and $+U$ is generated. This is consistent with the SJ images and the polarization direction observed during the 60–110 s time range (left panel of Figure 3.11). Conversely, when the slit is located on the left side of the spicule, radiation from the right side becomes weak, such that radiation from the left side becomes strong. In this case, $-U$ is generated. This is consistent with the polarization direction observed during the 200–250 s time range (right panel of Figure 3.11). When the slit is located in the middle of the spicule, radiation comes from the front side. In this case, the radiation from the right and left sides are equal, and U becomes zero, which is consistent with the polarization direction observed around 160 s (middle panel of Figure 3.11). From the above discussion, the temporal variation of U signal is considered as the effect that the observation position changed with respect to the spicule.

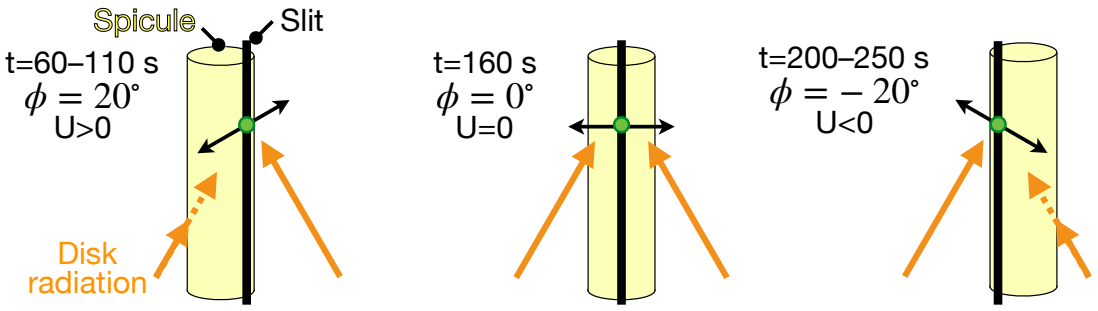

Figure 3.11: The relationship between the slit, spicule, and polarization direction in time.

If the above discussion is correct, if we could perform a spectropolarimetric observation in the Lyα line with a slit perpendicular to the spicule, we could observe the polarization direction being different on the left and right sides of the spicule structure. To derive the magnetic field semi-quantitatively, we have to model a non-axisymmetric radiation field. In this case, because only radiation from one side is considered, it can be approximated as a half cone ($0° < \chi < 180°$ in Figure 3.7). We have to consider not only J^0_0 and J^2_0, but also higher-order parameters, such as J^2_1 and J^2_2.

3.5 Summary and Conclusion

A spicule is a jet-like structure, which is most ubiquitously present in the chromosphere. As the structure that connects the photosphere and corona, it has been studied from the consideration of various mechanisms, such as those of spicule formation, energy transportation, and energy dissipation. In this consideration, the magnetic field of the spicule is the most basic and important physical quantity for its characterization. A few observational studies have derived the magnetic field of spicules; however, a comprehensive understanding of this magnetic field has remained elusive.

CLASP is a sounding rocket experiment that has succeeded in obtaining Lyα spectropolarimetric data from spicules for the first time. In this study, we tried to derive the magnetic field of the spicule using CLASP observational data. First, we found that a $90°$

scattering polarization (i.e., positive Q/I) is dominant in the Lyα off-limb spicule. This indicates that the radiation mainly comes from below and is symmetric around the spicule axis in the temporally averaged field. Second, we found the height variation of the polarization signal. The polarization degree is higher in the spicule upper-part ($Q/I = 0.5\%$) than in the lower-part ($Q/I = 0.2\%$). This is understood to be caused by the height variation in the radiation anisotropy. In the lower-part, because the spicule is dense, the radiation comes from not only the vertical but also the horizontal directions. Therefore the net polarization is small. However, in the upper-part, because the radiation comes from the vertical direction, the polarization is larger than in the lower-part. Third, we found that the U/I signal varies temporally from $+0.5\%$ to -0.5%. This is the first result that indicates the temporal variation of the polarization signal on a spicule, thanks to the CLASP high-throughput observations. This variation may be due to the temporal variations in the radiation field and/or the magnetic field resulting from the Hanle effect. To distinguish between these effects, we have semi-quantitatively modeled the radiation field, particularly considering the axisymmetric and non-axisymmetric fields, and compared the observed and calculated polarization signals. Based on the analytical results, we found that it is difficult to explain the observational results, e.g., the temporal variation of the polarization signal in the axisymmetric radiation field. In addition, we found that the period of the plane-of-sky oscillation of the spicule with respect to the slit position coincided with the temporal variation in the polarization signal. This can be explained qualitatively because, assuming that the Lyα line spicule is optically thick, the oscillation of the spicule causes a temporal variation in the non-axisymmetric radiation field at the slit position. Therefore, to derive the magnetic field of the Lyα line spicule, it is necessary to evaluate the non-axisymmetric radiation field, considering the spicule dynamics.

CLASP was launched again in April 2019 as the Chromospheric LAyer Spectro-Polarimeter (CLASP2; Narukage et al. 2016; Song et al. 2018; Yoshida et al. 2018), and the full Stokes vector (I, Q, U, and V) of the Mg II h & k lines near 280 nm was obtained. The Mg II k line at 279.6 nm is not only sensitive to the Hanle effect, like the Lyα line,

but also sensitive to the Zeeman effect, which is not affected by the radiation field because it has a longer wavelength than the Lyα line. In the future, more quantitative magnetic field derivations will be possible by simultaneously observing multiple spectral lines with different magnetic field sensitivities.

Chapter 4

Discussion and Summary

4.1 Energy Flux

This is the first and a very challenging study focused on deriving a magnetic field and velocity field simultaneously in the ultraviolet wavelength range, which will provide new insights into the theoretical model and lead to observation by satellites in the future. We found that spicules have a very dynamic structure and some physical quantities are related to the derivation of the physical quantities in a complex manner. In addition, this observation experiment has only obtained data for the very limited time of 5 min. Conversely, good observational data of 5 min can provide very interesting results. In the future, we will be able to understand the relationship between multiple physical quantities by conducting studies using long-term observation data from satellite observations and using multiple spectral lines with different magnetic field sensitivities.

Previous studies have suggested for the mechanism of energy transfer to the corona to be waves. From CLASP observations, we found high-frequency and low-frequency oscillations in the chromospheric spicules. In this section, we calculate the energy flux of the high-frequency and the low-frequency oscillations and discuss the effects on the corona.

4.1.1 High-Frequency Oscillation

We have found a high-frequency wave propagating along a spicule from high-resolution spectroscopic observations of CLASP for the first time. The wavelet analysis revealed that high-frequency waves with a period of about 30 s propagated upward with a velocity amplitude of $3\ \mathrm{km\ s^{-1}}$ and a propagation velocity of $470\ \mathrm{km\ s^{-1}}$. This propagation velocity is equal to the Alfvén velocity in the chromosphere ($100\ \mathrm{km\ s^{-1}}$; magnetic field strength of 10 G, and density of $7 \times 10^{-14}\ \mathrm{g\ cm^{-3}}$). Therefore, this wave can be regarded as the MHD wave. There are two possible modes of MHD waves: Alfvén wave, which is incompressible wave, and fast mode, which has compressibility. As the propagation velocities of these two modes are almost the same in the chromosphere, we did not identify the modes for the derivation of the energy flux. The solid line in Figure 4.1 shows the height variation of the velocity amplitude of the observed high-frequency wave. The uncertainty of the velocity amplitude obtained from the observation is $0.6\ \mathrm{km\ s^{-1}}$, which is attributed to the bisector analysis. The dashed line is the height variation of the velocity amplitude calculated using Equation (1.2) under the following three assumptions.

1. The magnetic field is constant in the height direction.

2. The density of the spicules decreases exponentially in the height direction (Figure 4.2).

3. Energy flux is preserved in the height direction.

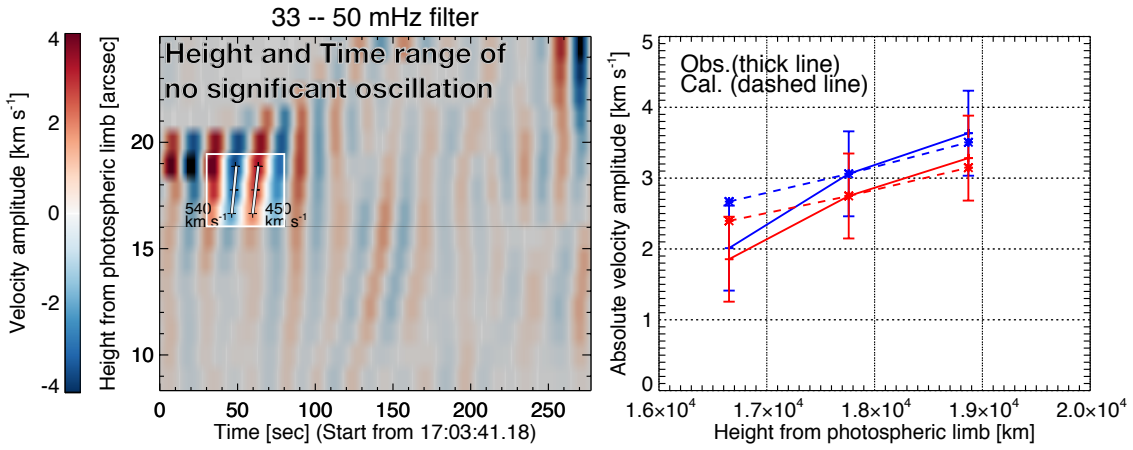

Figure 4.1: (Left) The results from the 30 s wave filter (33–50 mHz) with the gray mask showed no significant oscillation. The white lines and values indicate the phase velocity. (Right) Observed velocity amplitude (solid line) and calculated velocity amplitude (dashed line) as a function of height from a photospheric limb. The blue lines are the blue-shifted component of the left panel, and the red lines are the red-shifted component of the left panel, each of which is an absolute value. The dashed lines are the height variation of the velocity amplitude calculated using Equation (1.2), and assuming that the energy flux is preserved in height, calculated based on the observed propagation velocity and the velocity amplitude at a height of 1.78×10^4 km.

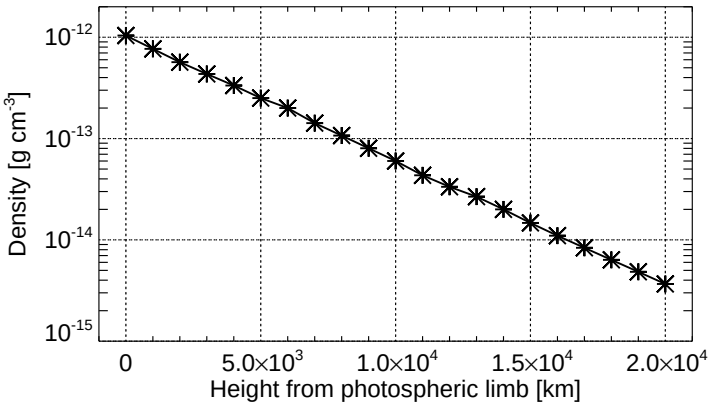

Figure 4.2: Spicule density as a function of height from photospheric limb. Figure adapted from Beckers (1968).

It is seen that the height variation between the observation result (solid line) and the calculation result (dashed line) is equal within the range of the error. Hence, it is seen that at this height, the energy flux of the wave propagates upward without dissipation. In contrast, an energy flux of the high-frequency wave (about 3×10^4 erg cm^{-2} s^{-1}) is smaller than the value required for heating the corona (about 3×10^5 erg cm^{-2} s^{-1}; Withbroe & Noyes 1977). However, it is conceivable that the velocity amplitude necessary for deriving the energy flux has been underestimated (see Section 2.4.3), or that the influence of the displacement between the oscillation direction and the line-of-sight direction has been underestimated.

4.1.2 Low-Frequency Oscillation

A low-frequency oscillation with a period of about 240 s was found from the Lyα line spectroscopic data and imaging data of CLASP. Figure 4.3 shows the temporal variation of the position X_{pos} of the spicule in the plane-of-sky (pos) and the line-of-sight (los) velocity V_{los}. In the SJ image, as the slit is located at the center of the spicule, it is difficult to quantitatively estimate the oscillation of the spicule in the pos, but it can be

seen that X_{pos} and V_{los} have a phase difference of $90°$. As this means that there is no phase difference between the pos velocity and the los velocity, it can be understood as a transverse kink mode oscillation. This indicates that this low-frequency oscillation is also a MHD wave with low compressibility. Further, it can be seen from Equation (4.1) that the inclination of the oscillation plane ψ with respect to the pos is $\psi = 44°$. We derived this value from the observed los velocity amplitude as $V_{los} = 20\ \mathrm{km\,s^{-1}}$, the observed oscillation period as $T = 240$ s, and the observed pos oscillation amplitude as $X_{pos} = 800$ km.

$$\psi = \tan^{-1}\left(\frac{V_{los}(t)}{\frac{dX_{pos}(t)}{dt}}\right) = \tan^{-1}\left(\frac{V_{los}}{X_{pos} \times 2\pi/T}\right) \tag{4.1}$$

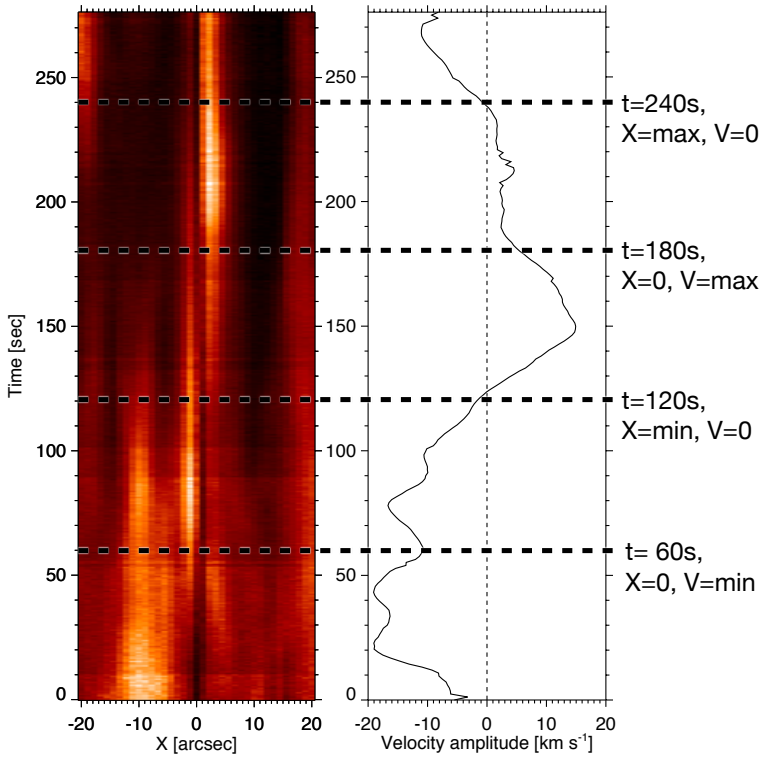

Figure 4.3: (Left) Temporal variation of the position X_{pos} of the spicule upper part in the plane-of-sky observed by SJ. This panel is as same as panel (g) of Figure 3.5. (Right) Line-of-sight velocity amplitude V_{los} as a function of time averaged in the spicule upper part observed by SP.

As the oscillation period of the low-frequency oscillation is similar to the observation time of CLASP, the propagation of this oscillation could not be investigated in detail. However, it can be seen from bottom right panel of Figure 2.4 that the phase of the oscillation (red and blue patterns) is shifted in the height direction. This phase difference matches that of the high-frequency wave which indicated by white arrows in this panel. Therefore, it is conceivable that the low-frequency oscillation propagates as a wave similar to the high-frequency wave. As the propagation velocity is determined by the density and the magnetic field in the medium and does not depend on the frequency, the propagation velocity of the low-frequency oscillation can be considered to

be the same as that of the high-frequency wave. The propagation velocity of the transverse kink mode is equal to the Alfvén velocity, if the density of the spicule is sufficiently higher than the surrounding density. The energy flux of the low-frequency wave can be obtained from the velocity amplitude as $V_{los}/\sin\psi = 29\ \mathrm{km\ s^{-1}}$ considering the inclination ψ of the oscillation plane, the propagation velocity ($470\ \mathrm{km\ s^{-1}}$), and the density as $6 \times 10^{-15}\ \mathrm{g\ cm^{-3}}$ (18 Mm height from the photosphere; Beckers 1968). The derived energy flux (about $2 \times 10^{6}\ \mathrm{erg\ cm^{-2}\ s^{-1}}$) is greater than the amount required to heat the quiet corona ($3 \times 10^{5}\ \mathrm{erg\ cm^{-2}\ s^{-1}}$; Withbroe & Noyes 1977).

The low-frequency wave is considered to originate from photospheric convection, because its oscillation period corresponds to the time scale of convective motion in the photosphere (Zaqarashvili & Erdélyi, 2009). In this case, as the low-frequency wave is generated regardless of the existence of the spicule, it is considered that the low-frequency wave can constantly contribute to the heating of the corona in various regions. In a region without a spicule, the density decreases but the velocity amplitude and the propagation velocity increase accordingly. Therefore, it is considered that a similar amount of energy can be transported in the chromosphere, regardless of the non-uniformity of the density. These observations have revealed the energy propagation process of waves in the chromosphere in detail. To investigate the contribution of this wave to the coronal heating in detail, it is necessary to examine the wave propagating in the corona in detail. In the corona, as the density is smaller than in the chromosphere, it is estimated that the wave propagation is observed as a value larger than the propagation velocity and the velocity amplitude value observed in the chromosphere this time.

Tomczyk et al. (2007) performed spectroscopic observations of the corona using a ground-based telescope and found wave propagation along a coronal loop. They reported that the wave propagates at a velocity of $2000\ \mathrm{km\ s^{-1}}$ and a velocity amplitude of $0.3\ \mathrm{km\ s^{-1}}$. The propagation velocity is greater than the value in the chromosphere, but the velocity amplitude is two orders of magnitude smaller than the value in the chromosphere. Furthermore, it has been reported that the energy flux ($10\ \mathrm{erg\ cm^{-2}\ s^{-1}}$) obtained

from these values is insufficient for heating the corona assuming the coronal density. In this observation, it is considered that the velocity amplitude was underestimated due to multiple velocity components overlapping in the line-of-sight (for details, see Chapter 2.4.1). Thus, sufficient wave energy flux has not been found in the corona. To understand the coronal heating mechanism, it is necessary to observe the chromosphere and corona simultaneously with high spatial resolution to investigate the propagation process of the low-frequency waves in more detail.

4.2 Future Prospects

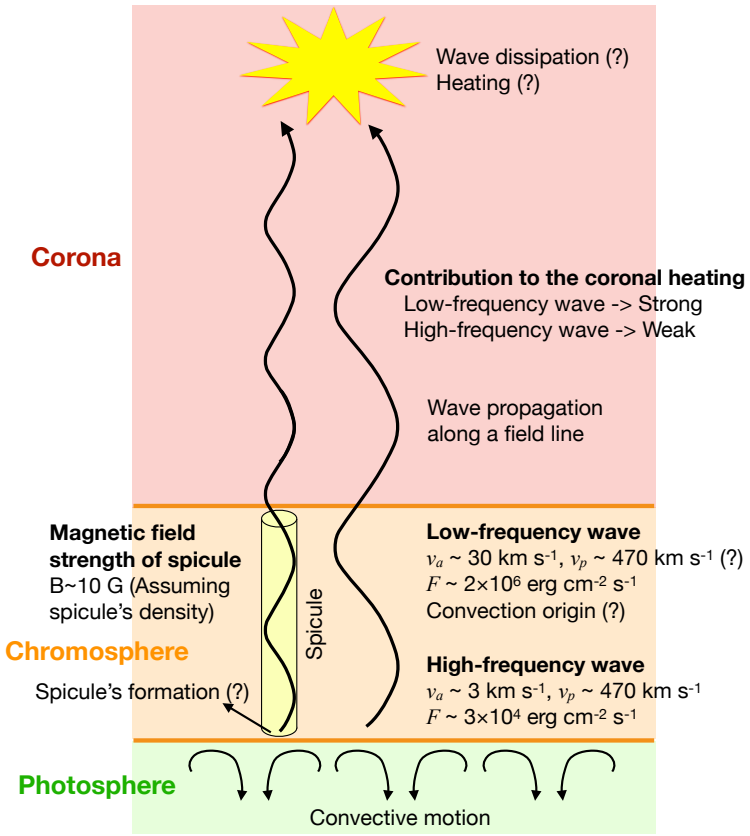

Figure 4.4: Summary of our findings and the remaining unknowns marked with question mark.

We summarize in Figure 4.4 what we did and did not find. From this study, the propagation process of the magnetic wave in the chromosphere was clarified more quantitatively than previous studies. However, to investigate their influence on the corona, it is necessary to seamlessly observe from the chromosphere to the corona and quantitatively evaluate the energy flux and energy dissipation of magnetic waves in the corona.

Solar-C_EUVST is the next solar observation satellite scheduled to be launched in early 2026, and will perform spectral observations of the chromosphere and corona simultaneously with high spatial and temporal resolution using multiple spectral lines sensitive to various temperatures. As a result, the energy flux and dissipative process of waves propagating from the chromosphere to the corona will be observed, and it is expected that the coronal heating mechanism can be investigated in detail. In particular, the Lyα line, whose usefulness was fully demonstrated by this observation, is the brightest among the spectral lines that *Solar-C_EUVST* will observe. Therefore, this analysis method and analysis result will be important for future research.

Furthermore, from the viewpoint of quantitatively deriving the energy flux propagating in the chromosphere, it is necessary to derive the magnetic field in the chromosphere. From analyzing the CLASP spectro-polarimetric data, it was found that the derivation of the magnetic field using the Lyα line requires modeling of the radiation field and considering non-axial symmetry. The Chromospheric LAyer Spectro-Polarimeter (CLASP2; Narukage et al. 2016; Song et al. 2018; Yoshida et al. 2018) is the second flight of CLASP and was launched on April 11, 2019 (Figure 4.5). In CLASP2, we conducted complete Stokes-vector (I, Q, U, and V) spectro-polarimetric observations in the Mg II h & k lines near 280 nm with the SP, while imaging observations in the Lyα line conducted with the SJ. In particular, the Mg II k line at 279.6 nm is sensitive to weaker magnetic fields than Lyα. In addition to the Hanle effect, the circular polarization induced by the Zeeman effect is measurable in Mg II h (280.4 nm) & k lines by sampling strong-field regions (Belluzzi & Trujillo Bueno, 2012; del Pino Alemán et al., 2016; Alsina Ballester et al., 2016). It may possible to detect foot-points of the spicule magnetic fields, as it is

important to understand the spicule formation and wave generation.

I participated in the CLASP2 project from the planning stage, and led the measurement of various optical elements, optical alignment of the telescopes (Yoshida et al., 2018), and evaluation of stray light. We have confirmed that the CLASP2 instrument has achieved the performance that meets the design requirements before and after the launch. Nearly all the calibrations have been completed, and the scientific results will be released soon. I have not started to analyze the scientific data yet, but it appears that the Stokes V signal caused by the Zeeman effect is likely to be obtained in the Mg II k lines; hence, we await more interesting results than that of CLASP.

Figure 4.5: CLASP2 launch. Credit: US Army Photo, White Sands Missile Range.

Appendix A

Appendix

A.1 Wavelet Analysis with Different Thresholds

Figure A.1 shows the wavelet analysis with different thresholds. Similar as the results of the 30% threshold (a and b), the oscillations of frequency 33–50 mHz are prominent in the time range of 0–100 s (c and e), and the oscillations of 19–27 mHz exist with a relatively longer duration than that of the oscillations of 33–50 mHz (d and f). The differences of the maximum wavelet power $9\ (\mathrm{km\ s^{-1}})^2$ in 30%, $14\ (\mathrm{km\ s^{-1}})^2$ in 40%, and $9\ (\mathrm{km\ s^{-1}})^2$ in 50% thresholds are consistent with the error of Doppler velocity $\sim 0.6\ \mathrm{km\ s^{-1}}$.

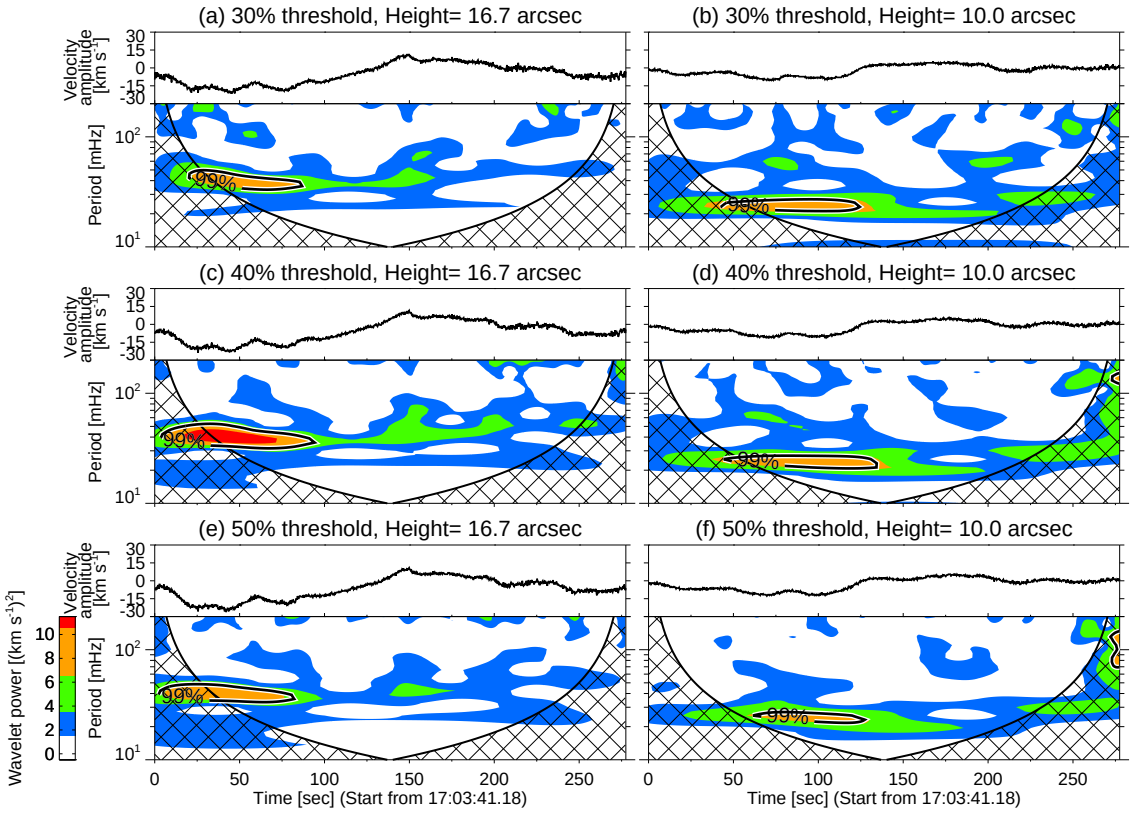

Figure A.1: The results of wavelet analysis and curves of Doppler velocity with a different thresholds of the bisector analysis and height. Top (a and b), middle (c and d), and bottom (e and f) panels correspond to a results of 30%, 40%, and 50% threshold, respectively. Left panels (a, c, and e) and right panels (b, d, and f) show the height $= 16.7$ arcsec and height $= 10.0$ arcsec, respectively.

References

Alfvén, H. 1947, MNRAS, 107, 211

Alissandrakis, C. E., Zachariadis, T., & Gontikakis, C. 2005, in ESA Special Publication, Vol. 11, The Dynamic Sun: Challenges for Theory and Observations, 54.1

Alsina Ballester, E., Belluzzi, L., & Trujillo Bueno, J. 2016, ApJL, 831, L15

Antolin, P., Okamoto, T. J., De Pontieu, B., Uitenbroek, H., Van Doorsselaere, T., & Yokoyama, T. 2015, ApJ, 809, 72

Aschwanden, M. J., Tarbell, T. D., Nightingale, R. W., Schrijver, C. J., Title, A., Kankelborg, C. C., Martens, P., & Warren, H. P. 2000, ApJ, 535, 1047

Auchère, F., Froment, C., Bocchialini, K., Buchlin, E., & Solomon, J. 2016, ApJ, 825, 110

Avrett, E. H., Fontenla, J. M., & Loeser, R. 1994, in IAU Symposium, Vol. 154, Infrared Solar Physics, ed. D. M. Rabin, J. T. Jefferies, & C. Lindsey, 35

Beckers, J. M. 1968, SoPh, 3, 367

Belluzzi, L., & Trujillo Bueno, J. 2012, ApJL, 750, L11

Belluzzi, L., Trujillo Bueno, J., & Štěpán, J. 2012, ApJL, 755, L2

Centeno, R., Trujillo Bueno, J., & Asensio Ramos, A. 2010, ApJ, 708, 1579

Chitta, L. P., van Ballegooijen, A. A., Rouppe van der Voort, L., DeLuca, E. E., & Kariyappa, R. 2012, ApJ, 752, 48

De Pontieu, B., et al. 2007, Science, 318, 1574

—. 2014, SoPh, 289, 2733

del Pino Alemán, T., Casini, R., & Manso Sainz, R. 2016, ApJL, 830, L24

del Toro Iniesta, J. C. 2003, Introduction to Spectropolarimetry

Deng, N., et al. 2015, ApJ, 799, 219

Edlén, B. 1943, ZAp, 22, 30

Gary, G. A. 2001, SoPh, 203, 71

Giono, G., et al. 2016a, in Society of Photo-Optical Instrumentation Engineers (SPIE) Conference Series, Vol. 9905, SPIE, 99053D

Giono, G., et al. 2016b, SoPh, 291, 3831

—. 2017, SoPh, 292, 57

Goto, M., Ishikawa, R., Iida, Y., & Tsuneta, S. 2019, Atoms, 7, 55

Gouttebroze, P., Lemaire, P., Vial, J. C., & Artzner, G. 1978, ApJ, 225, 655

Hahn, M., Landi, E., & Savin, D. W. 2012, ApJ, 753, 36

Hahn, M., & Savin, D. W. 2013, ApJ, 776, 78

Handy, B. N., et al. 1999, SoPh, 187, 229

He, J. S., Tu, C. Y., Marsch, E., Guo, L. J., Yao, S., & Tian, H. 2009, A&A, 497, 525

Hollweg, J. V., Jackson, S., & Galloway, D. 1982, SoPh, 75, 35

Hudson, H. S. 1991, SoPh, 133, 357

Ishikawa, R., Narukage, N., Kubo, M., Ishikawa, S., Kano, R., & Tsuneta, S. 2014, SoPh, 289, 4727

Ishikawa, R., & Tsuneta, S. 2009, A&A, 495, 607

Ishikawa, R., et al. 2013, ApOpt, 52, 8205

—. 2017a, ApJ, 841, 31

Ishikawa, S., et al. 2015, SoPh, 290, 3081

Ishikawa, S.-n., et al. 2017b, ApJ, 846, 127

Kano, R., et al. 2012, in Society of Photo-Optical Instrumentation Engineers (SPIE) Conference Series, Vol. 8443, SPIE, 84434F

Kano, R., et al. 2017, ApJL, 839, L10

Kato, Y., Steiner, O., Hansteen, V., Gudiksen, B., Wedemeyer, S., & Carlsson, M. 2016, ApJ, 827, 7

Kato, Y., Steiner, O., Steffen, M., & Suematsu, Y. 2011, ApJL, 730, L24

Kim, Y.-H., Bong, S.-C., Park, Y.-D., Cho, K.-S., Moon, Y.-J., & Suematsu, Y. 2008, Journal of Korean Astronomical Society, 41, 173

Kobayashi, K., et al. 2012, in Astronomical Society of the Pacific Conference Series, Vol. 456, Fifth Hinode Science Meeting, ed. L. Golub, I. De Moortel, & T. Shimizu, 233

Kosugi, T., et al. 2007, SoPh, 243, 3

Kubo, M., et al. 2016, ApJ, 832, 141

Kudoh, T., & Shibata, K. 1999, ApJ, 514, 493

Landi Degl'Innocenti, E., & Landolfi, M. 2004, Polarization in Spectral Lines, Vol. 307

Lemen, J. R., et al. 2012, SoPh, 275, 17

Lites, B. W., et al. 2008, ApJ, 672, 1237

López Ariste, A., & Casini, R. 2005, A&A, 436, 325

Matsumoto, T., & Kitai, R. 2010, ApJL, 716, L19

Matsumoto, T., & Suzuki, T. K. 2014, MNRAS, 440, 971

Matthaeus, W. H., Zank, G. P., Oughton, S., Mullan, D. J., & Dmitruk, P. 1999, ApJL, 523, L93

McIntosh, S. W., de Pontieu, B., Carlsson, M., Hansteen, V., Boerner, P., & Goossens, M. 2011, Nature, 475, 477

Narukage, N., Auchère, F., Ishikawa, R., Kano, R., Tsuneta, S., Winebarger, A. R., & Kobayashi, K. 2015, ApOpt, 54, 2080

Narukage, N., et al. 2011, SoPh, 269, 169

Narukage, N., et al. 2016, in Society of Photo-Optical Instrumentation Engineers (SPIE) Conference Series, Vol. 9905, Proc. SPIE, 990508

—. 2017, Soph, 292, 40

Okamoto, T. J., Antolin, P., De Pontieu, B., Uitenbroek, H., Van Doorsselaere, T., & Yokoyama, T. 2015, ApJ, 809, 71

Okamoto, T. J., & De Pontieu, B. 2011, ApJL, 736, L24

Okamoto, T. J., et al. 2007, Science, 318, 1577

Orozco Suárez, D., Asensio Ramos, A., & Trujillo Bueno, J. 2015, ApJL, 803, L18

Pasachoff, J. M., Jacobson, W. A., & Sterling, A. C. 2009, SoPh, 260, 59

Pereira, T. M. D., De Pontieu, B., & Carlsson, M. 2012, ApJ, 759, 18

Pereira, T. M. D., et al. 2014, ApJL, 792, L15

Pesnell, W. D., Thompson, B. J., & Chamberlin, P. C. 2012, SoPh, 275, 3

Samanta, T., et al. 2019, Science, 366, 890

Scharmer, G. B., Bjelksjo, K., Korhonen, T. K., Lindberg, B., & Petterson, B. 2003, in Society of Photo-Optical Instrumentation Engineers (SPIE) Conference Series, Vol. 4853, SPIE, ed. S. L. Keil & S. V. Avakyan, 341–350

Scharmer, G. B., et al. 2008, ApJL, 689, L69

Schou, J., et al. 2012, SoPh, 275, 229

Secchi, A. 1875, Le Soleil

Shimizu, T. 1995, PASJ, 47, 251

Shoda, M., & Yokoyama, T. 2018, ApJ, 854, 9

Singh, K. A. P., & Dwivedi, B. N. 2007, NewA, 12, 479

Song, D., et al. 2018, in Society of Photo-Optical Instrumentation Engineers (SPIE) Conference Series, Vol. 10699, Proc. SPIE, 106992W

Srivastava, A. K., et al. 2017, Scientific Reports, 7, 43147

Suematsu, Y., et al. 2008, SoPh, 249, 197

Teriaca, L., Schühle, U., Solanki, S. K., Curdt, W., & Marsch, E. 2006, in ESA Special Publication, Vol. 617, SOHO-17. 10 Years of SOHO and Beyond, 77

Tian, H., Curdt, W., Marsch, E., & Schühle, U. 2009, A&A, 504, 239

Tomczyk, S., & McIntosh, S. W. 2009, ApJ, 697, 1384

Tomczyk, S., McIntosh, S. W., Keil, S. L., Judge, P. G., Schad, T., Seeley, D. H., & Edmondson, J. 2007, Science, 317, 1192

Torrence, C., & Compo, G. P. 1998, Bulletin of the American Meteorological Society, 79, 61

Trujillo Bueno, J., Landi Degl'Innocenti, E., & Belluzzi, L. 2017, SSRv, 210, 183

Trujillo Bueno, J., Merenda, L., Centeno, R., Collados, M., & Landi Degl'Innocenti, E. 2005, ApJL, 619, L191

Trujillo Bueno, J., Štěpán, J., & Casini, R. 2011, ApJL, 738, L11

Tsiropoula, G., Tziotziou, K., Kontogiannis, I., Madjarska, M. S., Doyle, J. G., & Suematsu, Y. 2012, SSRv, 169, 181

Tsuneta, S., et al. 1991, SoPh, 136, 37

—. 2008, SoPh, 249, 167

Vernazza, J. E., Avrett, E. H., & Loeser, R. 1981, ApJS, 45, 635

Vögler, A., Shelyag, S., Schüssler, M., Cattaneo, F., Emonet, T., & Linde, T. 2005, A&A, 429, 335

Vourlidas, A., Sanchez Andrade-Nuño, B., Landi, E., Patsourakos, S., Teriaca, L., Schühle, U., Korendyke, C. M., & Nestoras, I. 2010, SoPh, 261, 53

Štěpán, J., & Trujillo Bueno, J. 2011, ApJ, 732, 80

Wilhelm, K., et al. 1995, SoPh, 162, 189

Withbroe, G. L., & Noyes, R. W. 1977, ARA&A, 15, 363

Yoshida, M., et al. 2018, in Society of Photo-Optical Instrumentation Engineers (SPIE) Conference Series, Vol. 10699, Proc. SPIE, 1069930

Yoshida, M., et al. 2019, ApJ, 887, 2

Yurchyshyn, V., Abramenko, V., & Goode, P. 2013, ApJ, 767, 17

Zaqarashvili, T. V., & Erdélyi, R. 2009, SSRv, 149, 355

Zaqarashvili, T. V., Khutsishvili, E., Kukhianidze, V., & Ramishvili, G. 2007, A&A, 474, 627

Acknowledgments

This PhD thesis is a summary of the study results that I have been worked in the Department of Astronomical Science, School of Physical Sciences, SOKENDAI (The Graduate University for Advanced Studies). Dr. Y. Suematsu was given the opportunity to carry out this study as a supervisor, and was given guidance throughout the process. I express my deepest gratitude here. Dr. R. Ishikawa and Dr. H. Hara were advised as well as guidance on the details of this paper. I express my deepest gratitude here.

I acknowledge the Chromospheric Lyman-Alpha Spectro-Polarimeter (CLASP) and Chromospheric LAyer Spectro-Polarimeter (CLASP2) teams, especially for Dr. R. Kano, Dr. M. Kubo, Dr. N. Narukage, Dr. Y. Katsukawa, Dr. D. Song, Dr. T. J. Okamoto, and Dr. J. Trujillo Bueno. The teams were an international partnership between NASA Marshall Space Flight Center, National Astronomical Observatory of Japan (NAOJ), Japan Aerospace Exploration Agency (JAXA), Instituto de Astrofísica de Canarias (IAC) and Institut d'Astrophysique Spatiale; additional partners include Astronomical Institute ASCR, Lockheed Martin, and University of Oslo. I am also grateful for the NAOJ staffs and students.

Finally, I would like to express my special thanks to my parents and my girl friend for their continuous support and encouragement. Thank you very much!